

1 **Decadal Evolution of Supraglacial Hydrology on the Nivlisen Ice Shelf:**
2 **From Localized Ponding to Spatially Synchronized Hydrofracture Forcing**
3 **(2015-2026)**

4 Geetha Priya M*, Charu Prabha R P, Y Mallikarjuna Madhav, Adithya Sunil,
5 Raina Bharathi, Deva Jefflin A R

6 Centre for Incubation Innovation Research and Consultancy (CIIRC), Jyothy Institute of Technology, Bengaluru
7 560082, Karnataka, India

8 *Corresponding author email id: geetha.sri82@gmail.com

9 **Abstract**

10 Understanding the mechanical response of Antarctic ice shelves to surface meltwater is
11 critical for evaluating their structural stability. This study presents 11 austral summer seasons
12 (AS 2015-2016 to AS 2025-2026) assessment of supraglacial melt pond dynamics and their
13 mechanical implications for the Nivlisen Ice Shelf grounding zone using Landsat-8/9 imagery
14 combined with in-situ validation from the 44th Indian Scientific Expedition to Antarctica
15 (ISEA-44). Supraglacial melt pond depths were retrieved from multispectral imagery and
16 integrated into an Euler–Bernoulli flexural framework to estimate bending stresses, hydrostatic
17 forcing, and the resulting stress intensity factors (K_{total}) across a network of ten major ponds.
18 Two prominent hydrological events were identified: an extreme localized ponding episode in
19 2017 (maximum depth 6.92 m) and a spatially extensive meltwater event in January 2026
20 characterized by high thickness normalized energy ($E_n = 97.81 \text{ MJ m}^{-1}$). Field validation using
21 a Keller DCX-22 pressure transducer indicates that satellite retrievals underestimate pond
22 depth by approximately 27.6% due to spatial averaging within 30 m pixels over concave pond
23 bathymetry. Despite this conservative bias, calculated stress intensities reach up to 0.61 MPa
24 $\text{m}^{1/2}$, exceeding the commonly reported fracture toughness range for glacier ice (0.1-0.4 MPa
25 $\text{m}^{1/2}$). These results suggest that episodic supraglacial melt ponding can generate stress
26 conditions favorable for hydrofracture initiation in the Nivlisen grounding zone sector. The
27 study demonstrates the value of combining long-term satellite observations with field
28 validation to assess the evolving mechanical vulnerability of Antarctic ice shelves.

29 **Keywords:** East Antarctica, Nivlisen Ice Shelf, Hydrofracture, Supraglacial melt pond, Stress
30 intensity factor.

31

32

33 **1. Introduction**

34 Ice shelves are floating extensions of the Antarctic Ice Sheet that play a critical role in
35 regulating the discharge of grounded ice into the ocean. By exerting a buttressing force on
36 upstream glaciers, ice shelves slow the flow of inland ice and thereby help stabilize the
37 Antarctic Ice Sheet. When ice shelves weaken or collapse, this buttressing effect is reduced,
38 allowing glaciers to accelerate and potentially increasing contributions to global sea level rise
39 (Morlighem et al., 2019; T. A. Scambos et al., 2004). One of the processes increasingly
40 recognized as a key driver of ice shelf instability is the formation and drainage of supraglacial
41 meltwater ponds and lakes. These surface water bodies can influence the mechanical stability
42 of ice shelves by promoting fracture propagation through hydrofracture processes (Banwell et
43 al., 2013; Bell et al., 2018).

44 Supraglacial melt ponds form when surface meltwater accumulates in topographic depressions
45 on glaciers or ice shelves during the austral summer melt season. The occurrence and
46 distribution of these lakes are controlled by surface energy balance, local topography, snow
47 permeability, and the presence of pre existing fractures (Jonathan Kingslake, 2017; Stokes et
48 al., 2019). Satellite observations have revealed widespread seasonal development of
49 supraglacial melt ponds across both the Antarctic and Greenland ice sheets, with increasing
50 evidence that their spatial extent and frequency are sensitive to climatic variability and
51 atmospheric warming (Arthur et al., 2020; Langley et al., n.d.; Murugesan et al., 2023). In
52 Antarctica, supraglacial melt ponds have been observed across several ice shelves in East and
53 West Antarctica, including the Amery, Shackleton, Roi Baudouin, and Larsen ice shelves
54 (Arthur et al., 2020; Bell et al., 2017; M & Venkatesh, 2024). These lakes can store significant
55 volumes of meltwater and may persist for extended periods before draining suddenly through
56 fractures.

57 The mechanical influence of supraglacial melt ponds on ice shelves arises primarily from two
58 mechanisms. First, the weight of ponded water imposes a vertical load on the ice surface,
59 generating flexural stresses within the ice shelf. Second, when water infiltrates surface
60 crevasses, the hydrostatic pressure of the water column can drive crack propagation through
61 the ice. This process, known as hydrofracture, occurs when water pressure within a fracture
62 exceeds the resisting stresses of the surrounding ice and allows the fracture to propagate
63 downward through the ice column (Alley et al., 2005; Veen, 1998). Hydrofracture has been
64 implicated as a key mechanism in the disintegration of several Antarctic ice shelves, most

65 notably the collapse of the Larsen B Ice Shelf in 2002, where extensive surface meltwater
66 ponding preceded rapid structural failure (Ayeal et al., 2003; T. A. Scambos et al., 2000) .

67 The propagation of fractures in ice is commonly analyzed using the framework of linear elastic
68 fracture mechanics (LEFM), in which the stress intensity factor (SIF) describes the magnitude
69 of stress concentration at the tip of a crack (Anderson, 2017). Fracture propagation occurs when
70 the applied stress intensity exceeds the fracture toughness of the material, denoted as (K_{IC}).
71 Laboratory and field measurements indicate that the fracture toughness of glacier ice typically
72 lies in the range of approximately $0.1\text{--}0.4 \text{ MPa m}^{1/2}$, depending on temperature, grain size, and
73 loading conditions (Rist et al., 2002; SCHULSON, 2011). In the context of supraglacial
74 hydrology, the total stress intensity acting at a crevasse tip may arise from multiple sources,
75 including bending stresses generated by pond loading, hydrostatic pressure from water filling
76 the crevasse, and the opposing lithostatic stress associated with the weight of the overlying ice
77 column.

78 Recent studies have highlighted the importance of understanding the coupling between
79 supraglacial hydrology and fracture mechanics in determining the structural stability of ice
80 shelves. Observational analyses have documented rapid drainage of supraglacial melt ponds
81 through hydrofracture, demonstrating that meltwater can penetrate through hundreds of meters
82 of ice within short timescales (Banwell et al., 2013; Lai et al., 2020). Numerical modelling and
83 remote sensing studies further suggest that increasing surface melt under a warming climate
84 could enhance hydrofracture susceptibility across several Antarctic ice shelves (Bell et al.,
85 2018; Pollard & Deconto, 2016). These findings underscore the need for quantitative
86 assessments of the mechanical forcing generated by supraglacial meltwater and its potential to
87 initiate fracture propagation.

88 Despite these advances, relatively few studies have combined observations of supraglacial melt
89 pond geometry with fracture mechanics based calculations to evaluate the stress intensities
90 generated by meltwater loading. Such analyses are important for determining whether
91 supraglacial melt ponds generate stresses capable of exceeding the fracture toughness of ice
92 and thus triggering hydrofracture. In this study, we investigate the fracture mechanical
93 implications of supraglacial melt pond loading by quantifying the gravitational potential energy
94 (GPE) associated with meltwater ponds and evaluating the resulting SIF acting on surface
95 fractures. By integrating satellite derived pond geometry with physically based calculations of
96 bending stresses, hydrostatic water pressure and lithostatic resistance, this work provides a

97 process-based assessment of the hydrofracture potential of supraglacial melt ponds and their
98 implications for the structural stability of Antarctic ice shelves.

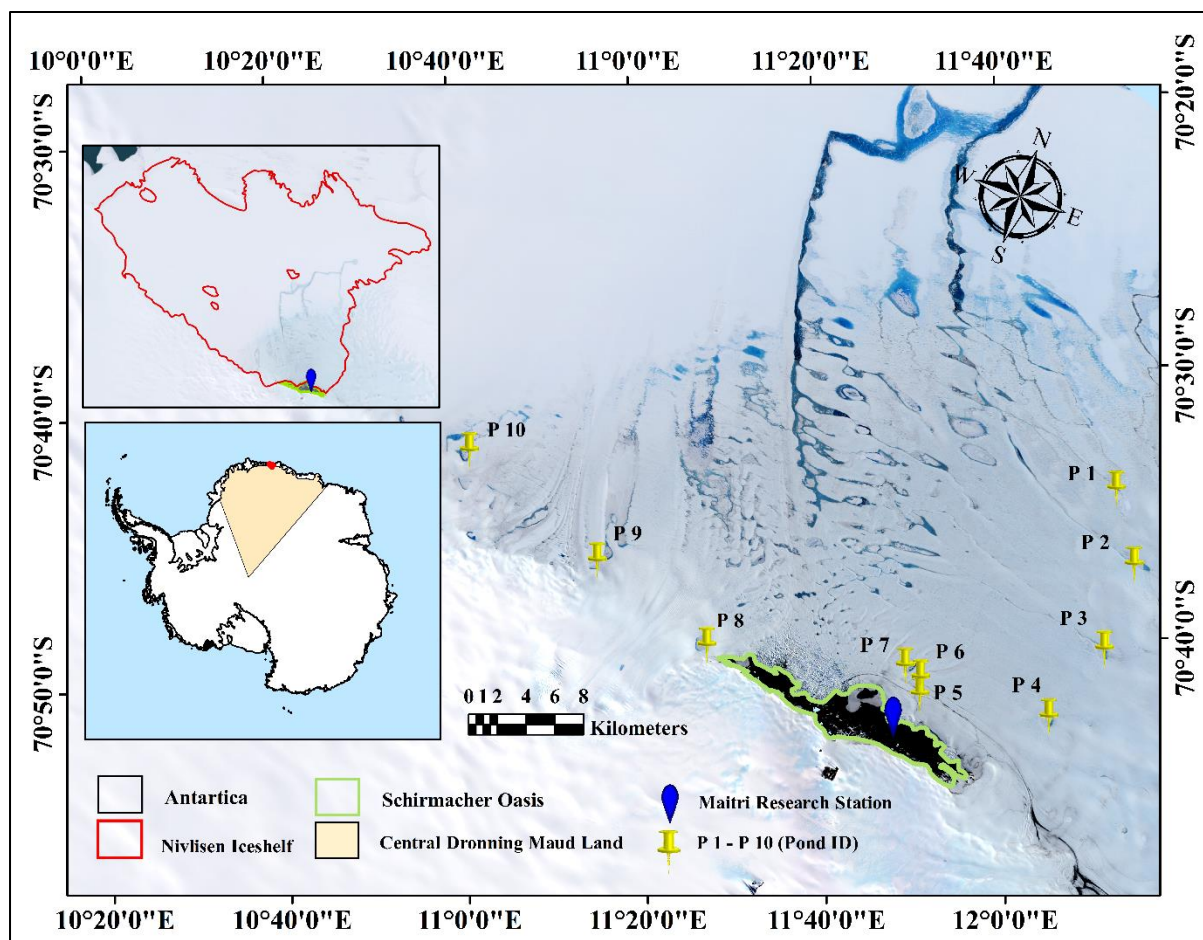
99 **2. Study Area**

100 The study is carried out on the Nivlisen Ice Shelf (NIS), located in Central Dronning
101 Maud Land (cDML), East Antarctica, in the vicinity of the Schirmacher Oasis along the
102 Princess Astrid Coast (Figure 1). cDML is a climatically and logistically well documented
103 sector of East Antarctica and hosts several long-term glaciological and geophysical
104 observations, making it particularly suitable for process oriented studies of ice ocean
105 atmosphere interactions and ice shelf stability (K. Mahalinganathan et.al, 2011).

106 A total of ten supraglacial melt ponds were selected on the NIS and labelled P1–P10. All ponds
107 exhibit irregular polygonal planform geometries and have end-to-end (maximum Feret)
108 diameters exceeding 250 m. This minimum diameter threshold of 0.25 km follows previous
109 hydrofracture and surface melt studies, which indicate that lakes of this linear scale are more
110 likely to contain the water volume necessary to generate mechanically significant water loading
111 or sustained fracture propagation (T. A. Scambos et al., 2000).

112 The distance of each pond from the grounding line was calculated as the shortest perpendicular
113 distance from the pond centroid to the nearest mapped grounding line. The selected ponds are
114 situated between 242 m (P9) and 2,791 m (P1) from the grounding line, thereby sampling a
115 mechanical gradient across the near-field sector of the ice shelf (Table 1). This configuration is
116 specifically designed to investigate hydrofracture processes ranging from the high flexure
117 grounding line (P9) to the outer limit of the grounding zone’s mechanical influence (P1), rather
118 than the freely floating interior of the shelf.

119 NIS in cDML was selected because multiple supraglacial melt ponds occur within a few
120 kilometres of a well defined grounding line, enabling a focused assessment of hydrofracture
121 under strong grounding zone bending stresses. In addition, this study is uniquely supported by
122 in-situ pond water depth and hydrostatic pressure measurements acquired during ISEA-44
123 (November 2024-January 2025) with logistics provided by National Centre for Polar and
124 Ocean Research (NCPOR) under the Ministry of Earth Sciences (MoES), Government of India
125 (GoI), which allows direct physical constraint of co-incident satellite based hydrofracture
126 modelling, ensuring that the simulated fracture mechanics are validated against real time
127 bathymetric and pressure states.



128

129 **Figure 1.** Study area map showing the location of selected 10 supraglacial melt ponds on the
 130 NIS, cDML, East Antarctica. (Base map- Landsat-8 imagery acquired on 28-01-2020)

131 **Table 1.** Distance of supraglacial melt ponds from the grounding line and corresponding local
 132 ice thickness derived from BedMachine v2.

S.no	Pond ID	Latitude, Longitude	Distance to the grounding line (m)	Local ice thickness (m)
1	P 1	-70.582477,12.054874	2791	519
2	P 2	-70.626066,12.129485	1979	655
3	P 3	-70.683820,12.093088	1007	639
4	P 4	-70.732944,12.016636	725	583
5	P 5	-70.729622,11.759308	651	393
6	P 6	-70.718715,11.755004	1161	409
7	P 7	-70.713614,11.736857	1337	390
8	P 8	-70.729676,11.335885	2296	446
9	P 9	-70.694339,11.112440	242	317
10	P 10	-70.640898,10.829409	1238	348

133

134 **3. Data used**

135 **3.1 Satellite imagery and pond mapping**

136 We analyzed 11 austral summer seasons (AS 2015-2016 to AS 2025-2026) using 19
137 cloud free scenes from Landsat-8 Operational Land Imager (OLI), Landsat-9 OLI2.
138 Although Sentinel-2 provides higher spatial resolution, it was not used to maintain consistency
139 across the full 2015–2026 period. Landsat 8/9 offer a continuous and radiometrically consistent
140 dataset, whereas incorporating Sentinel-2 (available only from ~2017) would introduce inter-
141 sensor variability due to differences in spatial and spectral characteristics. Scenes were filtered
142 for a maximum of 20% total scene cloud cover, with manual inspection conducted to ensure
143 all 10 target pond locations were cloud free in the selected acquisitions (Table 2).

144 The dataset distribution varies from one scene per season in the early study period to four
145 scenes per season in later years (Table 3). This multi temporal approach captures the ponds at
146 various stages of the melt cycle from November through February. In Table 3, "undetected
147 pond IDs" refers specifically to cloud obscuration or extensive fresh snow cover preventing a
148 clear observation of the ice surface, this distinction is critical to avoid underestimating pond
149 frequency in the presence of seasonal weather patterns (Arthur et al., 2020; M et al., 2022). To
150 delineate pond boundaries and estimate depth, we utilized the Blue (band 2) and Red (band 4)
151 30 m resolution bands. Specifically, we calculated the Normalized Difference Water Index for
152 ice ($NDWI_{ice}$) using both bands for robust surface water masking, while the Red band was
153 utilized for the radiative transfer model (RTM) for water depth estimation, following the
154 optimized single band approach for supraglacial melt ponds on East Antarctic ice shelves.
155 Sentinel-1 SAR imagery (C-band) from February 2015 onward was examined to assess the
156 persistence of supraglacial drainage structures across austral summer seasons.

157 **3.2 Ice thickness and BedMachine integration**

158 Ice thickness (H) for each pond centroid was extracted from the BedMachine Antarctica
159 v2 dataset (Morlighem et al., 2019). While BedMachine provides a 500 m gridded product,
160 thickness values were extracted using bilinear interpolation to derive thickness values
161 specifically at the pond centroids, minimizing discretization artifacts that arise when applying
162 a 500 m regional grid (BedMachine) to 250 m scale surface features.

163 We assigned a single, time invariant thickness value and grounding line position to each pond
164 for the duration of the study period. This assumption of stationarity is justified by the

165 glaciological stability of the NIS, which is characterized by slow flow velocities and negligible
 166 multi year thickness changes in cDML (K. Mahalinganathan et.al, 2011; Morlighem et al.,
 167 2019). Interannual thinning and grounding line migration in this sector are significantly smaller
 168 than the inherent vertical uncertainty of the BedMachine product and the 30 m horizontal
 169 resolution of the satellite imagery used for pond mapping. Consequently, these variations are
 170 treated as secondary to the high frequency hydrostatic and flexural stresses that drive seasonal
 171 hydrofracture, allowing for a consistent spatial baseline across the study period (Banwell et al.,
 172 2013).

173

174 **Table 2.** Landsat scenes used for supraglacial melt pond analysis, including satellite platform,

S.No	Satellite	Date	Scene_ID	Path	Row
1	LC08	01-01-2016	LC08_L1GT_167110_20160101_20201016_02_T2	167	110
2	LC08	21-12-2017	LC08_L2SR_167110_20171221_20201016_02_T2	167	110
3	LC08	04-02-2017	LC08_L2SR_167110_20170204_20201016_02_T2	167	110
4	LC08	24-12-2018	LC08_L2SR_167110_20181224_20201016_02_T2	167	110
5	LC08	28-01-2020	LC08_L2SR_167110_20200128_20201016_02_T2	167	110
6	LC08	13-12-2020	LC08_L2SR_167110_20201213_20210314_02_T2	167	110
7	LC08	10-01-2021	LC08_L2SR_167110_20210114_20210308_02_T2	167	110
8	LC08	14-11-2021	LC08_L2SR_167109_20211114_20211125_02_T2	167	110
9	LC09	24-12-2021	LC09_L2SR_167110_20211224_20230503_02_T2	167	110
10	LC09	25-11-2022	LC09_L1GT_167109_20221125_20230320_02_T2	167	110
11	LC09	27-12-2022	LC09_L1GT_167110_20221227_20230316_02_T2	167	110
12	LC09	28-01-2023	LC09_L1GT_167109_20230128_20230309_02_T2	167	110
13	LC08	21-02-2023	LC08_L1GT_167110_20230221_20230228_02_T2	167	110
14	LC09	30-12-2023	LC09_L1GT_167110_20231230_20231230_02_T2	167	110
15	LC08	01-07-2024	LC08_L1GT_167109_20240107_20240122_02_T2	167	110
16	LC08	24-02-2024	LC08_L2SR_167109_20240224_20240229_02_T2	167	110

17	LC08	09-01-2025	LC08_L1GT_167110_20250109_20250121_02_T2	167	110
18	LC09	19-12-2025	LC09_L2SR_167110_20251219_20251220_02_T2	167	110
19	LC09	06-01-2026	LC09_L2SR_165110_20260106_20260107_02_T2	165	110

175 product level, acquisition date, scene ID, path and row.

176 **Table 3.** Temporal record of satellite observations and visibility of supraglacial melt ponds
 177 during the study period.

Year	Date	Undetected Pond IDs
AS 2015-2016	01-01-2016	P 1,P6
AS 2020-2021	13-12-2020	P 5,P 6
AS 2020-2021	14-01-2021	P 1,P 5
AS 2021-2022	14-11-2021	P 1,P 3, P 5,P 6,P 10
AS 2022-2023	25-11-2022	P 1,P 10
AS 2022-2023	21-02-2023	P 1,P5
AS 2023-2024	12-11-2023	P 1,P 10
AS 2023-2024	30-12-2023	P 1,P 5,P 10
AS 2023-2024	07-01-2024	P 1,P 10
AS 2023-2024	24-02-2024	P 5,P 10

184

185

186 4. Methodology: Satellite preprocessing and melt-pond depth retrieval

187 The hydrofracture analysis was carried out for ten supraglacial melt ponds on the NIS,
 188 located near the Schirmacher Oasis, using multisensor satellite observations and a two-
 189 dimensional LEFM framework (Figure 2).

190 Surface reflectance Landsat-8, 9 scenes acquired during 11 austral summers were
 191 radiometrically and atmospherically pre processed. Melt pond depths (h) were retrieved
 192 following the RTM (equation 1) together with the NDWI_{ice} formulation (equation 2) and
 193 threshold values reported in the same study (Arthur et al., 2020; M et al., 2022).

$$194 \quad h = \frac{[\ln(A_v - R_d) - \ln(R_w - R_d)]}{c} \quad (1)$$

$$195 \quad NDWI_{ice} = \frac{(Blue\ band_{reflectance} - Red\ band_{reflectance})}{(Blue\ band_{reflectance} + Red\ band_{reflectance})} \quad (2)$$

196 Where, A_v is the average reflectance around pond boundary, R_d is the deep water reflectance
 197 (~ 0), R_w is the shallow water reflectance, c is the attenuation coefficient.

198 Additionally, $NDWI_{ice}$ thresholded rasters were converted to pond polygons in QGIS (Quantum
199 Geographic Information System) and used to mask the corresponding depth rasters. Zonal
200 statistics were then computed for each pond to obtain area, maximum depth, mean depth, and
201 pixel integrated water volume. To ensure bathymetric consistency across the 30 m resolution
202 grid, anomalous depth outliers were identified via the depth standard deviation and removed
203 prior to selecting final maximum depth values. The derived pond geometries and bathymetric
204 profiles serve as the primary inputs for the hydrofracture modelling framework, integrated with
205 the crack depth scenarios described below.

206 **4.1 Pre-existing crevasse assumption**

207 In this study, the terms crevasse, crack, and fracture refer to the same surface initiated
208 tensile discontinuity within the ice column. A pre existing near-surface crevasse is assumed to
209 exist beneath each supraglacial melt pond. Observational and theoretical studies show that
210 supraglacial melt ponds often occupy mechanically weakened or pre fractured zones and may
211 activate near surface crevasses during hydrofracture initiation (Banwell et al., 2013; T.
212 Scambos et al., 2009). The repeated formation of the same ponds across multiple austral
213 summers in our dataset suggests the presence of persistent structural weaknesses, supporting
214 this assumption.

215 As the subsurface geometry cannot be directly observed, the crack configuration is prescribed
216 following first order fracture mechanics treatments (Veen, 1998). We assume the crevasse
217 initially exists as a dry fracture. When a pond forms above it, water is assumed to infiltrate and
218 hydraulically connect with the crevasse. This converts the feature into a water filled fracture
219 where the net stress intensity (K_{total}) is determined by the superposition of hydrostatic water
220 pressure and the ambient glaciological stress field, specifically the bending induced tensile
221 stresses characteristic of the grounding zone.

222 To evaluate the sensitivity of hydrofracture potential to these combined stresses, three crack-
223 depth scenarios were considered: 10 m, 20 m, and 30 m. These represent (i) typical penetration
224 of dry crevasses, (ii) deeper penetration approaching the firm ice transition and (iii) a depth at
225 which water filled fractures may become mechanically unstable under the influence of flexural
226 loading and hydrostatic head, following first order analyses (Veen, 1998).

227

228

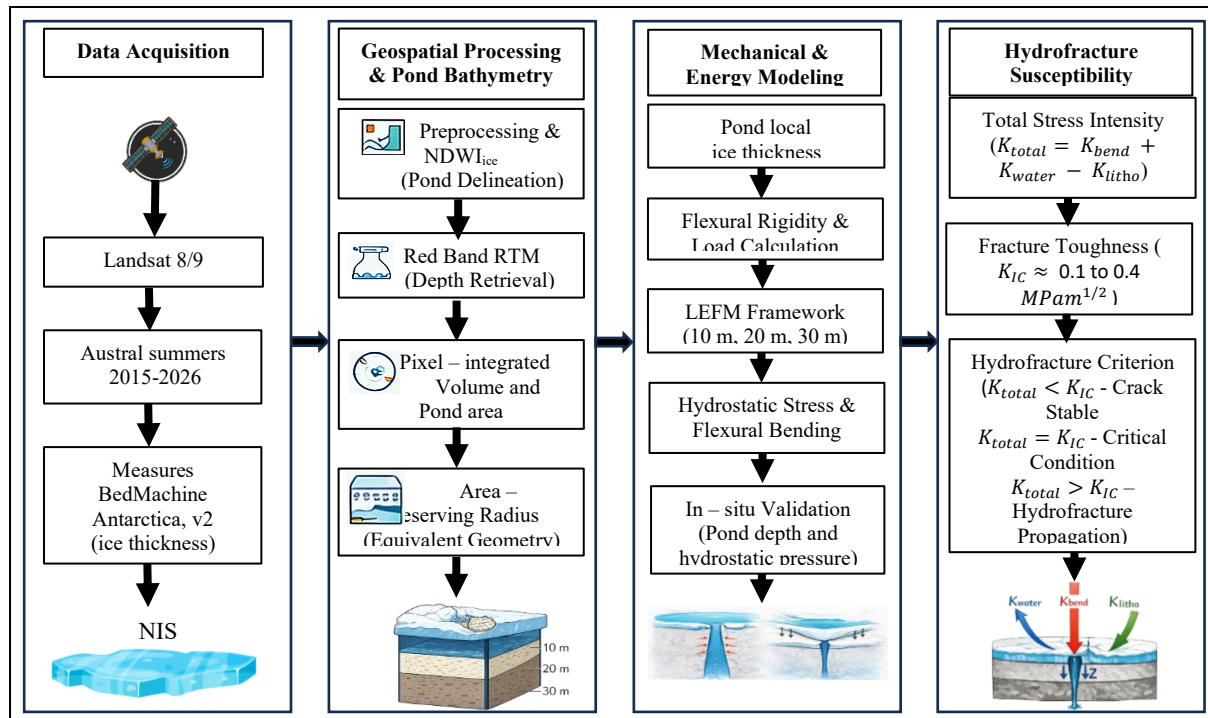


Figure 2. Process Flow

5. Hydrofracture modelling framework

5.1 LEFM formulation and plane strain assumption

A two-dimensional (2D) LEFM framework under plane strain conditions was used to evaluate the stability of the ten irregularly shaped melt ponds. This formulation is physically justified because observed pond diameters (>250 m) are an order of magnitude larger than the prescribed crack depths (10-30 m), allowing the central cross-section to be treated as effectively infinite in the out-of-plane direction (Krawczynski et al., 2009). The characteristic pond radius (r) is calculated from the area equivalent diameter (D_{eff}) (Equations 3-4) and used to define the lateral extent of the hydrostatic load. The 2D plane strain assumption provides a conservative estimate of the SIF by neglecting the three-dimensional "clamping" effects of a finite circular pond perimeter (Veen, 1998). LEFM is adopted in preference to viscous or viscoelastic formulations because the timescale of hydrofracture is significantly shorter than the Maxwell relaxation time of ice, such that the material response during loading is appropriately described as brittle elastic (CUFFEY, 2011; Veen, 1998).

$$r = \frac{D_{eff}}{2} \quad (3)$$

248
$$D_{eff} = 2 \sqrt{\frac{Pond\ Area}{\pi}} \quad (4)$$

249 **5.2 Grounding line flexure and bending stresses**

250 Although the study region lies approximately 50-90 km upstream of the calving front,
251 all analysed ponds are located close to the southern grounding line (242-2,791 m). The ice shelf
252 is therefore approximated as a clamped Euler-Bernoulli elastic beam within the grounding line
253 flexure zone, where semi diurnal tidal deflections of approximately 1.5 m exert a first order
254 control on the stress state of the ice shelf (G. Holdsworth, 1969; Vaughan, 1995). Due to the
255 large flexural rigidity, small vertical deflections are amplified into significant surface tensile
256 stresses at the grounding line hinge.

257 **5.3 Material properties**

258 To represent localized conditions near the Schirmacher Oasis, we adopted a depth
259 averaged ice density (ρ_i) of 850 kg m^{-3} and a Young's modulus (E) of $\sim 9 \text{ GPa}$ (Nimmo, 2004;
260 Sinharay, 2022). This density represents the depth integrated mean of the meteoric ice column,
261 accounting for the suppression of deep firn by katabatic wind scouring (Humbert et al., 2009).
262 The resulting stiff, brittle near-surface ice column is critical for assessing fracture initiation.
263 The adopted E value lies within the upper range for polycrystalline ice consistent with Ground
264 Penetrating Radar (GPR) and stratigraphy data from local blue ice areas (BIAs) (CUFFEY,
265 2011; Sinharay, 2022). This depth averaged approach ensures a robust estimate of lithostatic
266 overburden pressure (P_i) and resulting SIFs.

267 **5.4 Hydraulic loading and stress-intensity formulation**

268 For each pond, meltwater mass (M) and hydrostatic pressure (P_b) were calculated using
269 a freshwater density of 1000 kg m^{-3} . The hydraulic driving force is governed by the total head,
270 the sum of maximum retrieved pond depth h_{max} and the prescribed crack depth z . This total
271 head determines the hydrostatic SIF K_{water} (Veen, 1998). Bending stresses σ_f are incorporated
272 using a static bending coefficient $C = 0.15$. This formulation enables the explicit coupling of
273 satellite derived bathymetry with ice geometry from BedMachine Antarctica v2 (Arthur et al.,
274 2020; Morlighem et al., 2019; Murugesan et al., 2023). For each pond and crack depth scenario
275 (10 m, 20 m, and 30 m), the formulations summarized in Table 4 adapted from established
276 studies were used to compute hydrostatic pressure at the pond bottom and crack tip, GPE and
277 E_n along with surface load (q), flexural rigidity (D_f) and flexural length (l_f). Fracture stability

278 was evaluated using the SIFs due to water loading (K_{water}), bending (K_{bend}), and lithostatic
 279 pressure (K_{litho}), which were summed to obtain the total SIF (K_{total}).

280 **Table 4.** Summary of governing equations used to derive hydraulic, mechanical, and fracture
 281 parameters within the supraglacial melt pond hydrofracture framework.

S. No	Parameter	Governing Equation	Where
1	Hydrostatic Pressure at Pond Bottom (kPa)	$P_b = \rho_w g h_{max}$	$g = 9.81 \text{ m s}^{-2}$, h_{max} - maximum pond depth
2	Hydrostatic Pressure at Crack Tip (kPa)	$P_w = \rho_w g(z + h_{max})$	z - crack depth (assumed 10 m), h_{max} - maximum pond depth
3	Bending Stress (Pa)	$\sigma_f = \frac{6M_{max}}{H^2}$	M_{max} - maximum bending moment, H - ice thickness
4	Maximum Bending Moment (N)	$M_{max} = Cqr^2$ $If r < l_f \rightarrow M_{max} = 0.15qr^2$; $If r \geq l_f \rightarrow M_{max} = 0.15ql_f^2$	q - surface load l_f - flexural length
5	Gravitational Potential Energy (J)	$GPE = \rho_w gVz$	
6	Driving Hydrofracture Energy (J)	$E_{drive} = GPE \left(\frac{P_b}{P_w} \right)$	P_b - hydrostatic pressure at pond bottom, P_w - hydrostatic pressure at crack tip
7	Thickness-Normalized Energy (J m^{-1})	$E_n = \frac{E_{drive}}{H}$	
8	Ice Overburden Pressure (kPa)	$P_i = \rho_i gZ$	ρ_i - ice density (850 kg m^{-3}),
9	Surface load (Pa)	$q = \rho_w g h_{mean}$	H_{mean} - mean pond depth.
10	Flexural Rigidity (Nm)	$D_f = \frac{EH^3}{[12(1-\nu^2)]}$	E - Young's modulus ($9 \times 10^9 \text{ Pa}$), ν - Poisson's ratio (0.30)
11	Flexural Length (m)	$l_f = \left(\frac{D_f}{\rho_w g} \right)^{\frac{1}{4}}$	D_f - flexural rigidity
12	SIF from Bending ($\text{MPa m}^{1/2}$)	$K_{bend} = 1.12 \sigma_f \sqrt{\pi z}$	σ_f - bending stress,
13	SIF from Water Pressure ($\text{MPa m}^{1/2}$)	$K_{water} = \left[1.12(\rho_w g h_{max}) + \left(\frac{2}{\pi} \right) \rho_w g(z) \right] \sqrt{\pi z}$	h_{max} - maximum pond depth
14	SIF from Lithostatic Pressure ($\text{MPa m}^{1/2}$)	$K_{litho} = \left[\left(\frac{2}{\pi} \right) \rho_i gZ \right] \sqrt{\pi z}$	
15	Combined Stress Intensity Factor ($\text{MPa m}^{1/2}$)	$K_{total} = K_{bend} + K_{water} - K_{litho}$	K_{bend} - SIF from bending, K_{water} - SIF from water pressure, K_{litho} - SIF from lithostatic pressure

282

283 6.Results

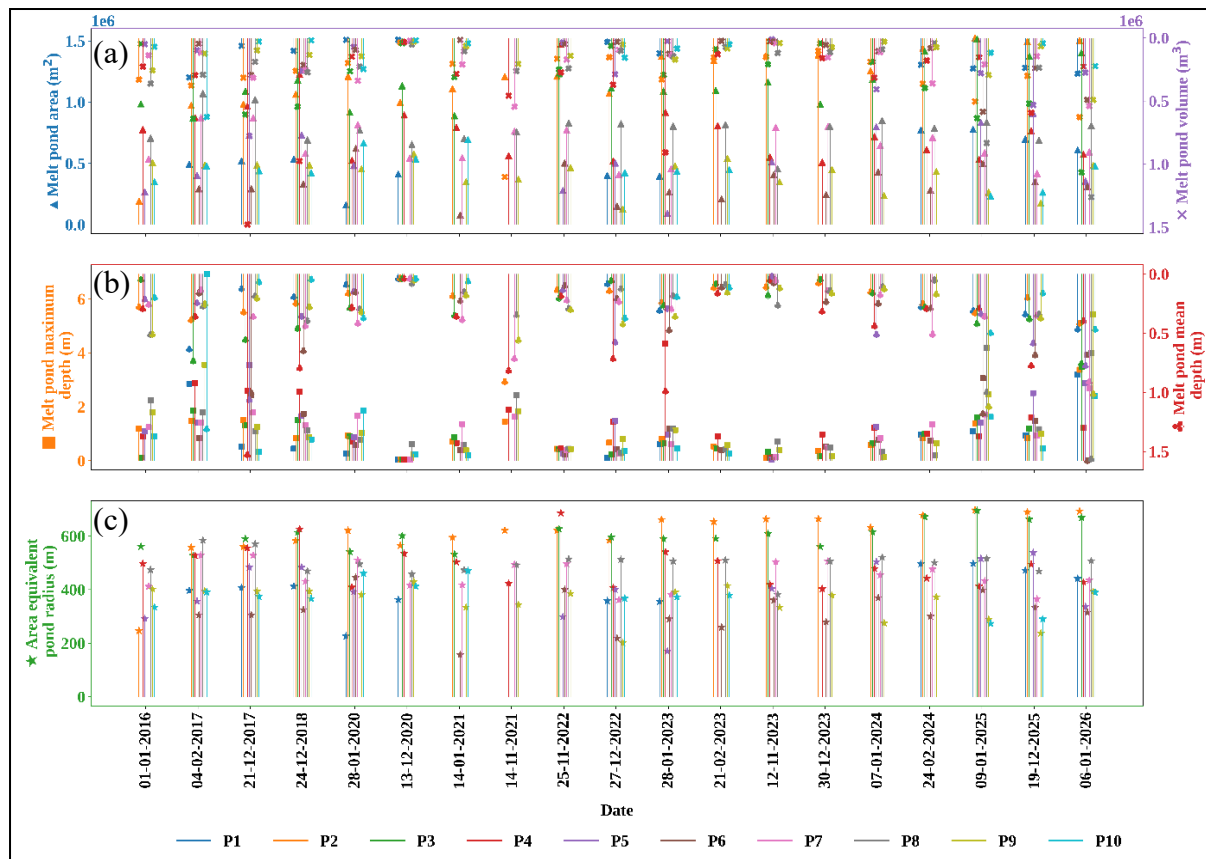
284 This section presents the morphometric, hydraulic and mechanical findings for the ten
 285 supraglacial melt ponds. Following the methodology established in Section 4, all parameters
 286 were evaluated across three crack depth scenarios (10 m, 20 m, and 30 m). This sensitivity
 287 framework allows for a direct comparison between the initial fracture state (10 m) and
 288 progressive hydrofracture scenarios (20-30 m), illustrating the shifting balance between

289 lithostatic overburden and hydrostatic driving pressure. These results are detailed across
290 Sections 6.1-6.6.

291 **6.1 Morphometric and bathymetric characteristics of supraglacial melt ponds**

292 Across 11 AS seasons, the ten analysed supraglacial melt ponds exhibit pronounced
293 spatial and temporal variability in surface area, depth, and water volume (Table 5; Figure 3).
294 Individual ponds were detected between 11 observations (P1) and 19 observations (P2, P4, P8,
295 and P9), reflecting differences in seasonal persistence as well as occasional cloud or snow
296 obscuration in the satellite record. Mean pond surface areas vary substantially between ponds,
297 ranging from 0.33 km² (P6) to 1.20 km² (P2). The largest individual pond recorded during the
298 study period occurred at P2, which reached 1.53 km² on 9 January 2025. Several other ponds
299 exhibit consistently large extents, particularly P3, P4, and P8, which maintain mean surface
300 areas exceeding 0.75 km² throughout the observation period. These observations indicate that
301 the NIS hosts multiple large and persistent supraglacial melt ponds capable of storing
302 substantial meltwater. Maximum pond depth (h_{\max}), retrieved using the RTM varies
303 considerably among ponds and between seasons. The mean of the seasonal maximum depths
304 for individual ponds ranges from 0.93 m (P3) to 1.49 m (P5). The deepest individual water
305 column in the dataset occurs at P10, reaching 6.92 m on 4 February 2017. Other episodically
306 deep ponds include P9 (5.43 m on 6 January 2026) and P4 (4.33 m on 28 January 2023),
307 demonstrating that significant deepening events can occur even in ponds that are not among
308 the largest by area. Meltwater storage volumes (V) show strong inter pond variability. Mean
309 pond volumes range from 0.13×10^6 m³ (P10) to 0.38×10^6 m³ (P4). The largest individual water
310 volume recorded in the dataset occurs at P4, which reached 1.48×10^6 m³ on 21 December 2017,
311 followed by P8, which stored 1.26×10^6 m³ on 6 January 2026. These mean and maximum
312 volumes represent statistics computed from all individual satellite observations available for
313 each pond. Spatially, ponds with the largest areas and volumes occur across the grounding zone
314 sector (242-2,791 m downstream of the hinge). While large ponds such as P2, P3, P4, and P8
315 are characterized primarily by extensive surface area and storage capacity, smaller pond such
316 as P10 which functions as a steep sided "well" or "moulin-like" feature can develop
317 episodically deep water columns. This highlights the importance of local pond geometry in
318 controlling meltwater accumulation on the NIS.

319



320

321 **Figure 3.** Temporal evolution of supraglacial melt pond geometry over eleven austral summers:
 322 (a) area and volume, (b) maximum and mean depth, and (c) area-equivalent radius.

323 **Table 5.** Morphometric and bathymetric characteristics of supraglacial melt ponds on the NIS
 324 during the study period.

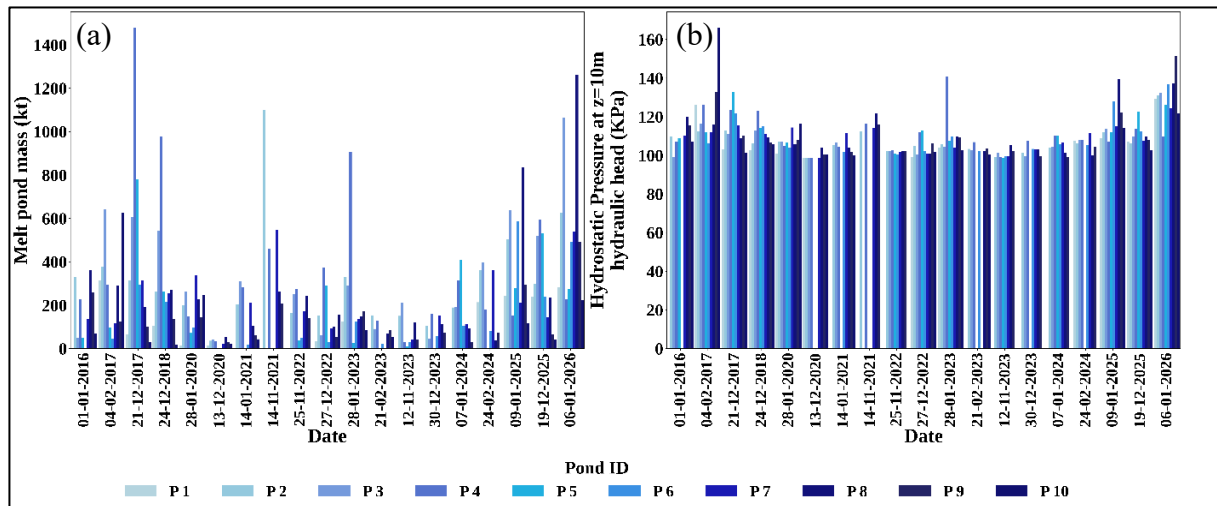
S.no	Pond ID	Mean Area (km ²)	Max Area (km ²)	Mean h _{max} (m)	Max h _{max} (m)	Mean Volume (km ³)	Max Volume (km ³)
1	P1	0.52	0.78	1	3.18	0.14	0.31
2	P2	1.2	1.53	0.95	3.37	0.31	0.63
3	P3	1.14	1.52	0.93	3.48	0.34	1.07
4	P4	0.77	1.48	1.38	4.34	0.38	1.48
5	P5	0.53	0.91	1.49	3.54	0.24	0.78
6	P6	0.33	0.62	1.18	3.92	0.16	0.59
7	P7	0.65	0.87	1.1	2.68	0.22	0.55
8	P8	0.78	1.07	1.27	4.2	0.26	1.26
9	P9	0.41	0.58	1.27	5.43	0.14	0.49
10	P10	0.45	0.69	1.3	6.92	0.13	0.63

325

326 **6.2 Derived hydraulic and geometric properties**

327 Using the geometries derived for the ten ponds (2015-2026), area equivalent radii (r)
328 were computed for each observation to serve as the lateral scale for water loading in the LEFM
329 formulation (equations 3-4). The radii range from 157 m (for P6 on 14 January 2021) to 697 m
330 (for P2 on 9 January 2025) (Table 6). Because these diameters are significantly larger than the
331 assumed crack depths (10-30 m), the conditions for the plane strain approximation are satisfied
332 (Veen, 1998).

333 Meltwater mass (M), derived using a freshwater density of 1000 kg m^{-3} , varies from 1.05×10^1
334 kt (for P5 on 12 November 2023) to 1.48×10^3 kt (for P4 on 21 December 2017). This mass
335 serves as the surface load for calculating flexural stresses. The total hydraulic head (H_w) acting
336 within the fracture is defined as the sum of maximum pond depth and crack depth ($H_w = h_{\text{max}}$
337 $+ z$) (Krawczynski et al., 2009; Veen, 1998). For the 10 m baseline, H_w ranges from 10.04 m
338 (for P2 on 13 December 2020) to 16.92 m (for P10 on 4 February 2017). At 30 m depth, H_w
339 increases to a maximum of 36.92 m. These water columns generate substantial hydrostatic
340 pressures. The pressure at the pond base (P_b) varies between 0.35 kPa (for P2 on 13 December
341 2020) and 67.93 kPa (for P10 on 4 February 2017). At the crack tip, pressure (P_w) increase
342 systematically with depth. For the 10 m scenario, P_w ranges from 98.45 kPa (for P2 on 13
343 December 2020) to 166.03 kPa (for P10 on 4 February 2017) as shown in Figure 4. For the 20
344 m and 30 m scenarios, pressure increase to 196.55 to 264.13 kPa and 294.65 to 362.23 kPa
345 respectively. The peak pressure consistently occurs at P10, reflecting its role as a deep
346 hydrostatic "well." These values provide the boundary inputs for the stress intensity analysis
347 in the following sections.



348 **Figure 4.** Temporal variability of (a) meltwater mass and (b) hydrostatic pressure at the crack
 349 tip ($z = 10$ m hydraulic head).

350 **Table 6.** Min/max hydraulic and geometric parameters for melt ponds P1-P10

S.no	Parameter	Min value	Pond ID	Date	Max value	Pond ID	Date
1	Area-equivalent pond radius	157 m	P6	14-01-2021	697 m	P2	09-01-2025
2	Meltwater mass	1.05×10^1 kt	P5	12-11-2023	1.48×10^3 kt	P4	21-12-2017
3	Hydraulic head (10 m crack)	10.04 m	P2	13-12-2020	16.92 m	P10	04-02-2017
4	Hydraulic head (20 m crack)	20.04 m	P2	13-12-2020	26.92 m	P10	04-02-2017
5	Hydraulic head (30 m crack)	30.04 m	P2	13-12-2020	36.92 m	P10	04-02-2017
6	Hydrostatic pressure (pond base)	0.35 kPa	P2	13-12-2020	67.93 kPa	P10	04-02-2017
7	Crack-tip pressure (10 m crack)	98.45 kPa	P2	13-12-2020	166.03 kPa	P10	04-02-2017
8	Crack-tip pressure (20 m crack)	196.55 kPa	P2	13-12-2020	264.13 kPa	P10	04-02-2017
9	Crack-tip pressure (30 m crack)	294.65 kPa	P2	13-12-2020	362.23 kPa	P10	04-02-2017

351

352

353

354

355 **6.3 Flexural and mechanical response to supraglacial melt pond loading**

356 The mechanical response of the NIS was quantified using surface water loads, bending
357 moments (M_{\max}), and bending stresses (σ_f) derived for individual observations between 2015
358 and 2026 (Table 7; Figure 5). These parameters define the elastic flexure induced by the
359 hydrostatic weight of ponded meltwater.

360 **6.3.1 Surface loading and bending moments**

361 Surface loading spans nearly two orders of magnitude across the dataset. The lowest
362 load occurs for P5 (202 Pa on 12 November 2023), while the highest reaches 1.55×10^4 Pa (for
363 P6 on 6 January 2026) reflecting extensive supraglacial meltwater accumulation. Several
364 seasons exhibit particularly strong mechanical forcing. For example, the AS of 21 December
365 2017 shows elevated loads across multiple ponds, including P4 (1.50×10^4 Pa) and P5 ($1.04 \times$
366 10^4 Pa).

367 This variability is mirrored in the maximum bending moments (M_{\max}), which reflect seasonal
368 meltwater production and pond geometry. The smallest moment was recorded at P5 on 12
369 November 2023 (4.93×10^6 N), whereas the largest historically occurred at P4 on 21 December
370 2017 (6.93×10^8 N). The 6 January 2026 event marks a significant intensification of mechanical
371 forcing compared to the relatively stable 2020-2025 period, with bending moments reaching
372 5.92×10^8 N at P8 and 4.99×10^8 N at P3. These 2026 values represent a sharp intensification
373 of mechanical forcing compared to the relatively stable years of 2020-2025, signalling a return
374 to conditions that favor structural instability.

375 **6.3.2 Bending stress and spatial rigidity**

376 The bending moments (σ_f) translate into surface tensile stresses that contribute to
377 fracture initiation. Across all observations, σ_f remains below the typical tensile strength of
378 glacier ice (approximately 0.7-1.0 MPa), but fluctuates significantly. The maximum bending
379 stress in the dataset occurs at P9 on 24 December 2018 (3.77×10^{-2} MPa). While 2018 produced
380 the single highest localized stress, the 6 January 2026 season represents a more spatially
381 extensive event; several ponds simultaneously experienced elevated stresses, including P8
382 (1.78×10^{-2} MPa) and pond P9 (1.37×10^{-3} MPa). This spatially coherent loading affects a
383 larger portion of the shelf surface simultaneously, which may be more critical for overall
384 stability than isolated maxima.

385 These responses are governed by the shelf's elastic properties. Flexural rigidity varies between
386 2.63×10^{16} Nm (for P9 on 6 January 2026) and 2.32×10^{17} Nm (for P2 on 1 January 2016),
387 reflecting spatial differences in ice thickness and stiffness. The corresponding flexural length

388 ranging from 1280 m (P9) to 2205 m (P2) remains constant for each pond location, confirming
389 that the mechanical sensitivity of each pond is pre determined by its glaciological position
390 relative to the grounding line.

391 **6.3.3 Mechanical implications for stability**

392 The extreme ponding events of December 2017, 2018 and January 2026 represent peak
393 periods of mechanical forcing. While the 2017 event produced the largest bending moments
394 (structural deformation), the 2018 event maximized localized bending stress (fracture risk).
395 Crucially, the 2026 event demonstrates a widespread mechanical response across ponds P3,
396 P6, P7, P8, P9, and P10 (Table 7). Although individual bending stresses remain an order of
397 magnitude below the failure threshold for intact ice, such repeated seasonal loading
398 progressively modifies the local stress field (Banwell et al., 2013; Veen, 1998). When these
399 flexural stresses are coupled with high internal water pressures, as seen in the 2017 and 2026
400 seasons, the conditions for hydrofracture initiation and the reactivation of dormant surface
401 fractures are significantly enhanced.

402

403

404

405

406

407

408

409

410

411
412
413
414
415
416
417
418
419
420
421
422
423
424
425
426
427
428
429
430
431
432
433
434
435
436
437
438
439
440
441
442
443
444

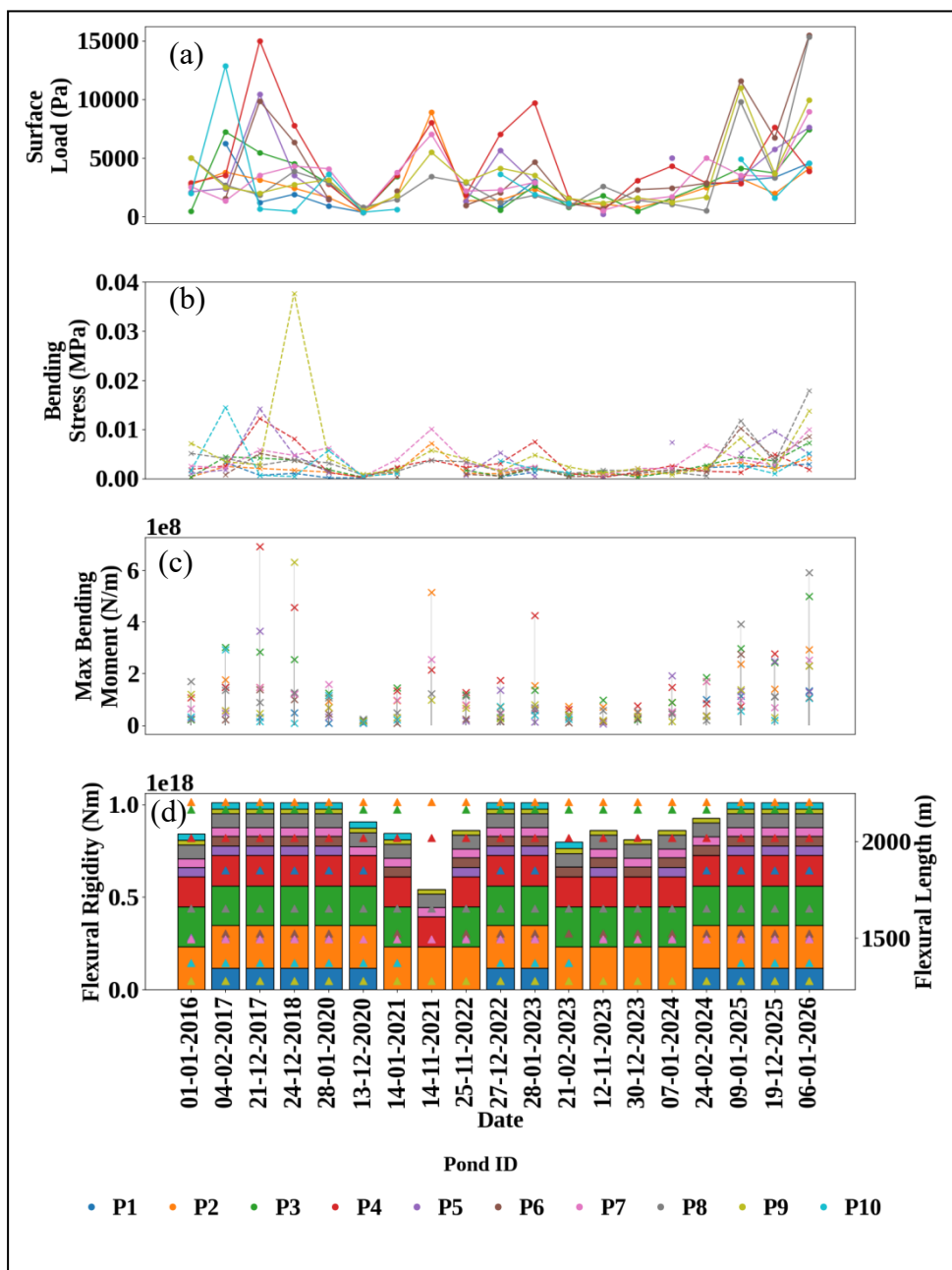


Figure 5. Mechanical response to supraglacial melt pond loading over eleven austral summers: (a) surface load, (b) bending stress, (c) maximum bending moment, and (d) flexural rigidity and flexural length.

445 **Table 7.** Mechanical parameters associated with supraglacial melt pond loading.

S.no	Parameter	Min value	Pond ID	Date	Max value	Pond ID	Date
1	Surface load	202 Pa	P5	12-11-2023	1.55×10^4 Pa	P6	06-01-2026
2	Maximum bending moment	4.93×10^6 N m ⁻¹	P5	12-11-2023	6.93×10^8 N m ⁻¹	P4	21-12-2017
3	Bending stress	1.54×10^{-4} MPa	P1	28-01-2020	3.77×10^{-2} MPa	P9	24-12-2018
4	Flexural rigidity	2.63×10^{16} Nm	P9	All dates	2.32×10^{17} Nm	P2	All dates
5	Flexural length	1280 m	P9	All dates	2205 m	P2	All dates

446

447 **6.4 Energetic potential for hydrofracture**

448 The energetic potential for hydrofracture was assessed by comparing the GPE stored
 449 within supraglacial melt ponds with the lithostatic resistance (P_i) imposed by the ice
 450 overburden. Three representative crack depth scenarios were considered: 10 m, 20 m, and 30
 451 m, corresponding to overburden pressures of 83.39 kPa, 166.77 kPa, and 250.16 kPa,
 452 respectively (Table 8; Figure 6).

453 **6.4.1 Gravitational Potential Energy**

454 The calculated GPE values relative to the crack tip span over two orders of magnitude
 455 across the observational record. The minimum recorded energy occurs at P5 on 12 November
 456 2023, where the GPE reaches 1.03×10^3 MJ (10 m), 2.06×10^3 MJ (20 m) and 3.10×10^3 MJ
 457 (30 m). In contrast, the largest energetic event is observed at P4 on 21 December 2017, when
 458 the GPE reaches 145.08×10^3 MJ (10 m), 290.15×10^3 MJ (20 m) and 435.23×10^3 MJ (30
 459 m). These values represent the maximum meltwater energy storage observed in the dataset and
 460 highlight the significant mechanical loading imposed by large supraglacial melt ponds.

461 Other high energy episodes are also evident. On 14 November 2021, P2 reached 107.97×10^3
 462 MJ (10 m), indicating a major meltwater accumulation event. Similarly, the 6 January 2026
 463 event produced elevated energies across several ponds, including P8 with 123.83×10^3 MJ and
 464 P3 with 104.55×10^3 MJ under the 10 m scenario. These events demonstrate that large energy
 465 storage episodes recur throughout the observational record and can involve multiple ponds
 466 simultaneously.

467

468 **6.4.2 Effective and thickness normalized driving energy**

469 The driving energy (E_{drive}) represents the fraction of stored GPE available for fracture
470 propagation after overcoming ice overburden pressure and mechanical resistance. To reveal the
471 true intensity of this hydraulic forcing while filtering out the influence of variable shelf
472 geometry, we utilize the E_n , measured in MJ m^{-1} .

473 Under the 10 m thickness scenario, E_{drive} ranges from a minimum of 4.18 MJ (for P5 on 12
474 November 2023) to a maximum of 35.33×10^3 MJ (for P8 on 6 January 2026). While minimum
475 values remain nearly identical across three crack depth scenarios (approximately 4.19 MJ at
476 P5), the peak E_{drive} values scale with thickness, reaching 41.22×10^3 MJ (20 m) and $43.64 \times$
477 10^3 MJ (30 m) during the January 2026 event at P8.

478 The thickness normalised energy follows a similar trajectory. For the 10 m scenario, E_n ranges
479 from a negligible 1.06×10^{-2} MJ m^{-1} to a peak of 79.21 MJ m^{-1} at P8 on 6 January 2026. For
480 thicker ice conditions (20 m and 30 m), these peak intensities increase to 92.39 MJ m^{-1} and
481 97.81 MJ m^{-1} at P8 on 6 January 2026 respectively. Notably, the 6 January 2026 event produced
482 elevated driving intensities across the pond network simultaneously under the 10 m scenario,
483 E_n reached 53.40 MJ m^{-1} (P9), 42.23 MJ m^{-1} (P3), and 33.86 MJ m^{-1} (P6). This synchronicity
484 suggests that high magnitude energetic forcing is not restricted to isolated ponds but occurs as
485 a system wide response.

486 **6.4.3 Energetic implications for system wide stability**

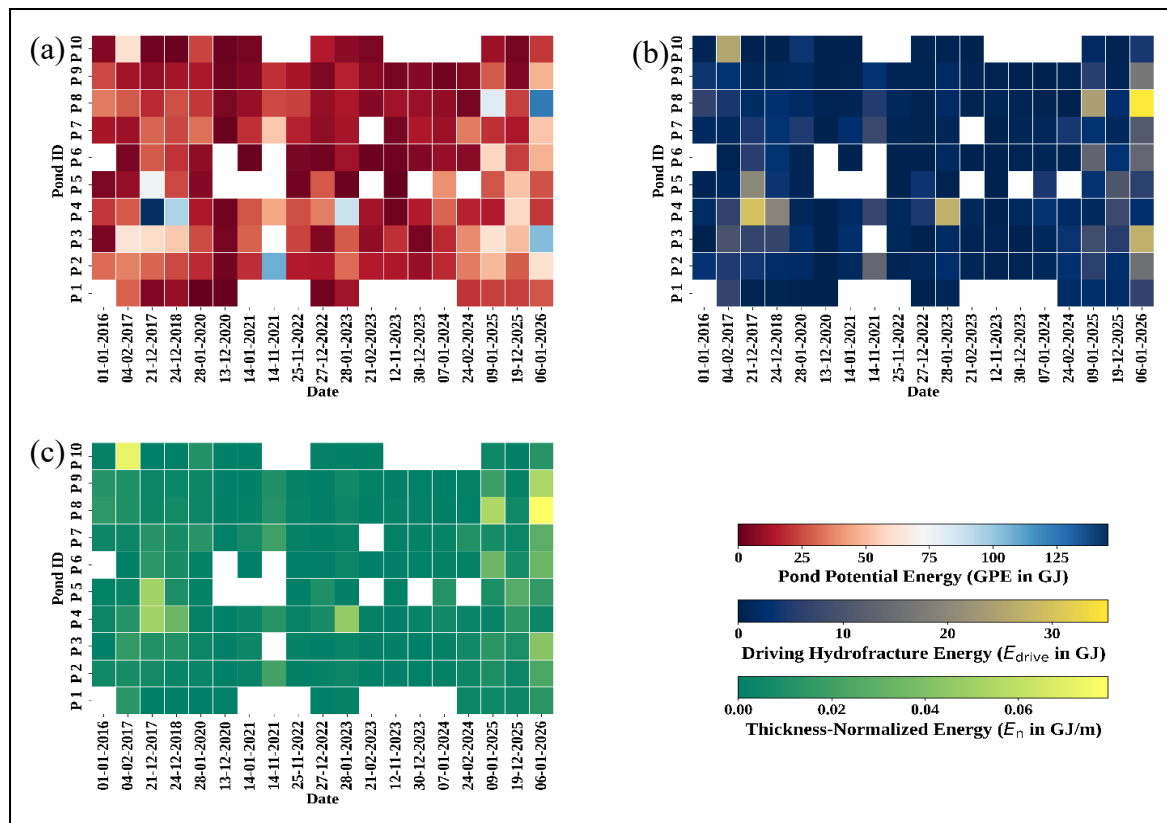
487 The 6 January 2026 event represents the most spatially extensive energetic forcing
488 episode observed in the record. While the 21 December 2017 peak at P4 reflects an extreme
489 energy concentration within a single large pond, the 2026 event is characterized by multiple
490 ponds simultaneously reaching high E_n values.

491 This spatial coherence suggests that meltwater loading was distributed across the pond network
492 rather than localized to a single pond. Consequently, the 2026 melt season represents the
493 strongest system wide hydrofracture forcing episode in the dataset, with multiple supraglacial
494 melt ponds approaching their maximum energetic potential. Such conditions substantially
495 increase the likelihood of widespread fracture initiation and propagation across the NIS,
496 emphasizing the critical role of pond scale meltwater dynamics in controlling ice shelf stability.

497

498

499



500

501 **Figure 6.** Temporal evolution of gravitational potential energy, hydrofracture driving energy
 502 and thickness-normalized energy.

503

504 **Table 8.** Energetic parameters governing hydrofracture potential of supraglacial melt ponds.

505

S.no	Parameter	10 m crack	20 m crack	30 m crack	Pond ID & Date
1	Maximum Absolute GPE	145.08× 10 ³ MJ	290.15× 10 ³ MJ	435.23× 10 ³ MJ	P4 – 21 Dec 2017
2	Minimum Absolute GPE	1.03× 10 ³ MJ	2.06× 10 ³ MJ	3.10× 10 ³ MJ	P5 – 12 Nov 2023
3	Maximum Driving hydrofracture energy (E _{drive})	35.33× 10 ³ MJ	41.22× 10 ³ MJ	43.64× 10 ³ MJ	P8 – 06 Jan 2026
4	Minimum Driving hydrofracture energy (E _{drive})	4.18 MJ	4.19 MJ	4.19 MJ	P5 – 12 Nov 2023
5	Maximum Thickness normalized energy(E _n)	79.21 MJ m ⁻¹	92.39 MJ m ⁻¹	97.81 MJ m ⁻¹	P8 – 06 Jan 2026
6	Minimum Thickness normalized energy (E _n)	1.06 × 10 ⁻² MJ m ⁻¹	1.07 × 10 ⁻² MJ m ⁻¹	1.07 × 10 ⁻² MJ m ⁻¹	P5 – 12 Nov 2023

506

507 **6.5 Fracture mechanics: Stress intensity and hydrofracture Potential**

508 The fracture potential associated with supraglacial melt pond loading was evaluated
509 using SIFs representing bending stresses (K_{bend}), hydrostatic water pressure (K_{water}), lithostatic
510 resistance (K_{litho}), and the resulting combined stress intensity (K_{total}). Representative stress
511 intensity values for major supraglacial melt pond events are summarized in Table 9, while the
512 highest values across the full dataset are identified in Tables 10-12.

513 **6.5.1 Bending induced stress intensity**

514 Flexural loading from pond water produces bending stresses within the ice shelf that
515 contribute to crack tip stress intensity. The largest bending event in the dataset occurred on 24
516 December 2018 at P9, where K_{bend} 10 m reached 0.2365 MPa m^{1/2} (Table 10). This value is
517 substantially larger than other bending events and reflects an extreme flexural response caused
518 by localized pond loading. Other high K_{bend} events include P8 on 6 January 2026 (0.1119 MPa
519 m^{1/2}) and Pond 10 on 4 February 2017 (0.0911 MPa m^{1/2}).

520 These results indicate that bending stresses can become significant when large supraglacial
521 melt ponds impose concentrated loads on the ice shelf surface. However, the largest bending
522 stresses generally occur at individual ponds rather than across multiple ponds simultaneously.

523 **6.5.2 Hydraulic forcing from meltwater**

524 Hydrostatic water pressure within crevasses produces the largest stress intensity
525 contribution in many events (Banwell et al., 2013; Veen, 1998). The strongest hydraulic forcing
526 occurs during the 4 February 2017 event at P10, where K_{water} 10 m reached 0.8204 MPa m^{1/2}
527 (Table 11). Additional high hydraulic forcing events occur at P9 on 6 January 2026 (0.7286
528 MPa m^{1/2}) and P4 on 28 January 2023 (0.6610 MPa m^{1/2}). Elevated values are also observed
529 during the 09 January 2025 melt event at P8 (0.6524 MPa m^{1/2}).

530 Unlike bending stresses, which tend to peak at individual locations, the 6 January 2026 event
531 produced elevated K_{water} values across several ponds simultaneously, indicating a spatially
532 distributed meltwater forcing episode.

533 **6.5.3 Combined stress intensity and fracture propagation**

534 The combined SIF (K_{total}) represents the net crack tip forcing produced by supraglacial
535 melt pond loading after accounting for the resisting effect of the overlying ice. In this
536 formulation, the total stress intensity is obtained by combining the bending induced stress
537 intensity (K_{bend}) and the hydrostatic water pressure contribution (K_{water}), while subtracting the
538 lithostatic resistance of the ice (K_{litho}) as given in Table 4.

539 The lithostatic term K_{litho} represents the compressive stress exerted by the weight of the
540 overlying ice column, which acts to resist fracture opening. In this study, K_{litho} is calculated
541 based on the assumed crack depth and remains constant for a given thickness scenario. For the
542 10 m crack depth case shown in Table 9, $K_{\text{litho}} = 0.299 \text{ MPa m}^{1/2}$. This resisting stress partially
543 offsets the bending and hydraulic contributions, meaning that fracture propagation occurs only
544 when the combined forcing from K_{bend} and K_{water} exceeds the lithostatic resistance of the ice.
545 The largest combined stress intensity occurs during the 4 February 2017 event at P10, where
546 $K_{\text{total 10 m}}$ reached $0.6124 \text{ MPa m}^{1/2}$ (Table 12). Other major events include P9 on 6 January
547 2026 ($0.5155 \text{ MPa m}^{1/2}$) and P8 on the same date ($0.4527 \text{ MPa m}^{1/2}$). Additional high combined
548 stress intensities occur during the 9 January 2025 melt event at P8 ($0.4273 \text{ MPa m}^{1/2}$) and 28
549 January 2023 at P4 ($0.4091 \text{ MPa m}^{1/2}$) (Figure 7). These events represent the most
550 mechanically favorable conditions for fracture propagation within the observational record.

551 **6.5.4 Comparison with ice fracture toughness**

552 To assess whether these stress intensities are sufficient to initiate fracture propagation,
553 the calculated values were compared with the fracture toughness of glacier ice (K_{IC}).
554 Experimental studies typically report K_{IC} values in the range of approximately 0.1-0.4 MPa
555 $\text{m}^{1/2}$ for glacier and ice shelf ice (Lai et al., 2020; Veen, 1998). Stress intensities exceeding this
556 range indicate conditions under which crack propagation becomes mechanically feasible.
557 Several events identified in Tables 9-12 exceed or approach this threshold. The 4 February
558 2017 P10 event ($K_{\text{total}} = 0.612 \text{ MPa m}^{1/2}$) clearly surpasses the upper bound of typical fracture
559 toughness. Similarly, the 6 January 2026 events at P8 and P9 ($K_{\text{total}} = 0.453$ and 0.516 MPa
560 $\text{m}^{1/2}$) exceed the fracture toughness range. Even the bending dominated 24 December 2018
561 event at P9 ($K_{\text{total}} = 0.384 \text{ MPa m}^{1/2}$) approaches the upper limit of this threshold.

562 **6.5.5 Implications for hydrofracture development**

563 The stress intensity analysis indicates that hydrofracture forcing on the NIS arises from
564 the combined effects of localized flexural loading and meltwater driven hydraulic
565 pressurization. Early extreme events in the record are typically associated with individual
566 ponds generating strong bending stresses, whereas more recent events show simultaneous
567 hydraulic forcing across multiple ponds, particularly during the 6 January 2026 melt episode.
568 When stress intensities exceed the fracture toughness of ice, downward crack propagation
569 becomes mechanically favorable, increasing the likelihood that supraglacial meltwater ponds
570 may trigger hydrofracture within the ice shelf.

571 **Table 9.** SIFs for major supraglacial melt pond events on the NIS, including contributions from
 572 bending (K_{bend}), hydrostatic water pressure (K_{water}), lithostatic resistance (K_{litho}) and the
 573 resulting total SIF (K_{total}) evaluated at a crack depth of 10 m.

S.no	Event	Pond ID	Date	K_{bend} (Mpa m ^{1/2})	K_{water} (MPa m ^{1/2})	K_{total} (MPa m ^{1/2})
1	Extreme hydrostatic forcing	P10	04-02-2017	0.0911	0.8204	0.6124
2	Extreme flexural bending	P9	24-12-2018	0.2365	0.4469	0.3844
3	Regional melt event	P8	09-01-2025	0.0740	0.6524	0.4273
4	System-wide forcing	P6	06-01-2026	0.0539	0.6355	0.3904
5	System-wide forcing	P8	06-01-2026	0.1119	0.6399	0.4527
6	Maximum fracture intensity	P9	06-01-2026	0.0860	0.7286	0.5155

574

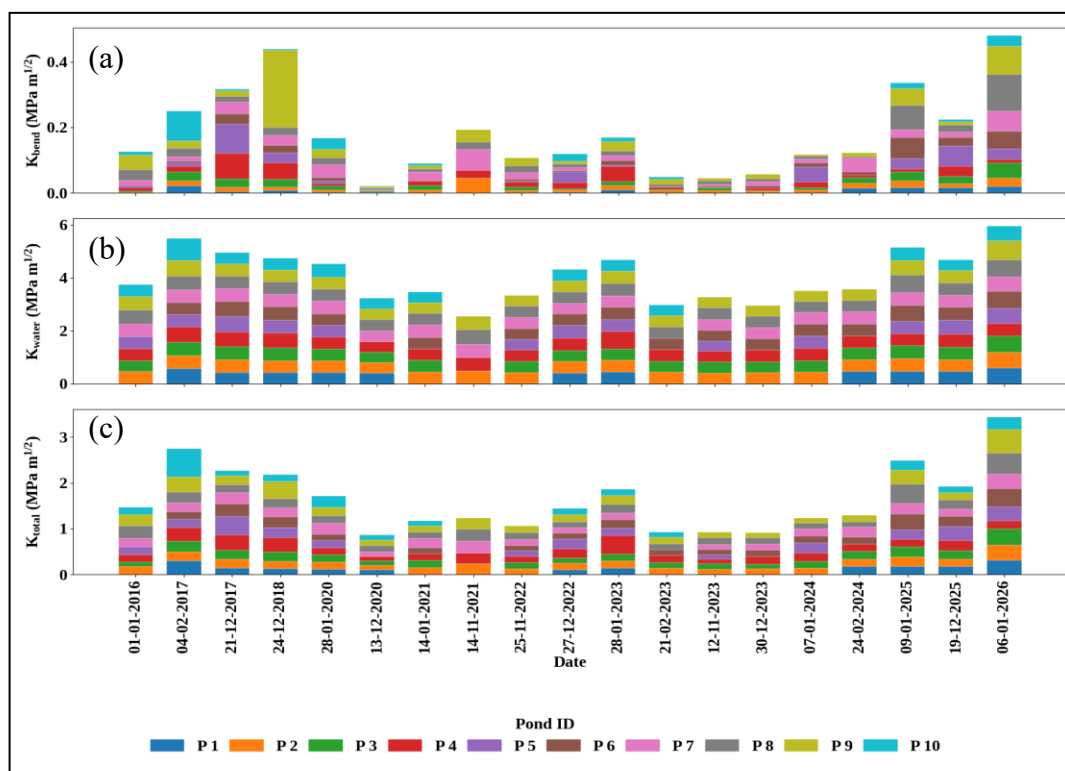
575 **Table 10.** Leading K_{bend} values among analysed supraglacial melt ponds.

S.no/Rank	Date	Pond ID	K_{bend} 10 m (MPa m ^{1/2})	K_{bend} 20 m (MPa m ^{1/2})	K_{bend} 30 m (MPa m ^{1/2})
1	24-12-2018	P 9	0.2365	0.3345	0.4097
2	06-01-2026	P 8	0.1119	0.1583	0.1939
3	04-02-2017	P 10	0.0911	0.1289	0.1578
4	21-12-2017	P 5	0.0889	0.1258	0.1541
5	06-01-2026	P 9	0.0860	0.1216	0.1490
6	21-12-2017	P 4	0.0768	0.1086	0.1330
7	09-01-2025	P 8	0.0740	0.1046	0.1281
8	09-01-2025	P 6	0.0643	0.0910	0.1114
9	14-11-2021	P 7	0.0633	0.0895	0.1096
10	06-01-2026	P 7	0.0626	0.0885	0.1084

576 **Table 11.** Leading K_{water} values among analysed supraglacial melt ponds

S.no/ Rank	Date	Pond ID	K_{water} 10 m (MPa $\text{m}^{1/2}$)	K_{water} 20 m (MPa $\text{m}^{1/2}$)	K_{water} 30 m (MPa $\text{m}^{1/2}$)
1	04-02-2017	P 10	0.8204	1.7174	2.7859
2	06-01-2026	P 9	0.7286	1.5876	2.6269
3	28-01-2023	P 4	0.6610	1.4921	2.5099
4	09-01-2025	P 8	0.6524	1.4798	2.4949
5	06-01-2026	P 8	0.6399	1.4621	2.4732
6	06-01-2026	P 6	0.6356	1.4561	2.4658
7	04-02-2017	P 9	0.6130	1.4241	2.4267
8	21-12-2017	P 5	0.6121	1.4228	2.4251
9	06-01-2026	P 3	0.6083	1.4176	2.4186
10	06-01-2026	P 2	0.6015	1.4079	2.4068

577



590 **Figure 7.** SIFs associated with supraglacial melt pond loading: (a) bending-induced (K_{bend}),
 591 (b) hydrostatic water pressure-induced (K_{water}) and (c) combined (K_{total}) over eleven austral
 592 summers.

593 **Table 12.** Leading K_{total} values among analysed supraglacial melt ponds.

S.no/Rank	Date	Pond ID	K_{total} 10 m (for $k_{litho}=0.2990$ $Mpa\ m^{1/2}$)	K_{total} 20 m (for $k_{litho}=0.8458$ $Mpa\ m^{1/2}$)	K_{total} 30 m (for $k_{litho}=1.5538$ $Mpa\ m^{1/2}$)
1	04-02-2017	P 10	0.6124	1.0005	1.3898
2	06-01-2026	P 9	0.5155	0.8634	1.2220
3	06-01-2026	P 8	0.4527	0.7746	1.1132
4	09-01-2025	P 8	0.4273	0.7386	1.0692
5	28-01-2023	P 4	0.4091	0.7130	1.0377
6	21-12-2017	P 5	0.4020	0.7028	1.0253
7	06-01-2026	P 6	0.3904	0.6865	1.0053
8	24-12-2018	P 9	0.3844	0.6780	0.9949
9	06-01-2026	P 3	0.3553	0.6368	0.9445
10	09-01-2025	P 6	0.3475	0.6258	0.9310

594

595 **6.6 Structural persistence, Hydrological activation, and Energy-driven melt channel**
 596 **transition**

597 Multi-temporal optical (Landsat-8/9) and Sentinel-1 SAR (Synthetic Aperture Radar)
 598 analysis indicates that the supraglacial melt channel over the NIS is governed by a persistent
 599 structural framework with episodic hydrological activation. Sinuous meltwater pathways
 600 observed in optical imagery (cerulean veins) correspond to melt channel structures consistently
 601 identifiable in Sentinel-1 SAR data from February 2015 onward. The analysis is restricted to
 602 AS seasons from 2015 to 2026, corresponding to the availability of Sentinel-1 SAR
 603 observations (Murugesan et al., 2023; Geetha Priya et al., 2024; Murugesan et al. 2025). The
 604 recurring presence of three melt channels in SAR indicates a stable, structurally controlled melt
 605 channel template.

606 In contrast, optical expression is temporally variable. On 6 January 2026, only two melt
 607 channels are clearly visible, whereas a third melt channel becomes observable on 12 January
 608 2026. Given its persistence in SAR across multiple years, this melt channel represents a pre
 609 existing pathway that becomes hydrologically active under increased meltwater availability,
 610 rather than a newly formed feature.

611 A further transition is observed on 21 January 2026, when a localized, circular to elliptical dark
 612 feature appears at a junction within the network and persists through mid February. Its position
 613 at a flow convergence point suggests localized concentration of hydraulic head within the
 614 network.

615 Selected melt ponds analysis were reliably derived only up to 6 January 2026, when pond
616 geometries remain well defined and the system is storage dominated. Beyond this date, ponds
617 exhibit blurring, drainage, snow burial, and contraction, preventing robust delineation. This
618 loss of discrete pond geometry reflects a transition from localized energy storage to distributed
619 drainage, rather than a data limitation.

620 The timing of this transition coincides with (i) activation of the third melt channel and (ii)
621 emergence of the localized drainage feature (Figure 8), indicating a threshold response to
622 increasing meltwater energy. Once storage capacity is exceeded, meltwater is redistributed
623 through the pre existing channel network, enhancing connectivity and concentrating flow at
624 nodal points. This redistribution is likely enhanced over low permeability ice surfaces, where
625 limited firn storage promotes rapid surface routing along structurally controlled pathways.

626 This progression from confined storage (≤ 6 January) to network activation and nodal
627 concentration (> 6 January) has direct mechanical implications. Concentration of meltwater at
628 junctions increases local hydraulic head and promotes stress amplification along pre existing
629 fractures, creating favorable conditions for incipient hydrofracture or crack propagation, even
630 where no through penetrating fracture is yet detectable. Thus, peak energy conditions drive a
631 transition from passive storage to active redistribution, increasing the likelihood of localized
632 structural weakening.

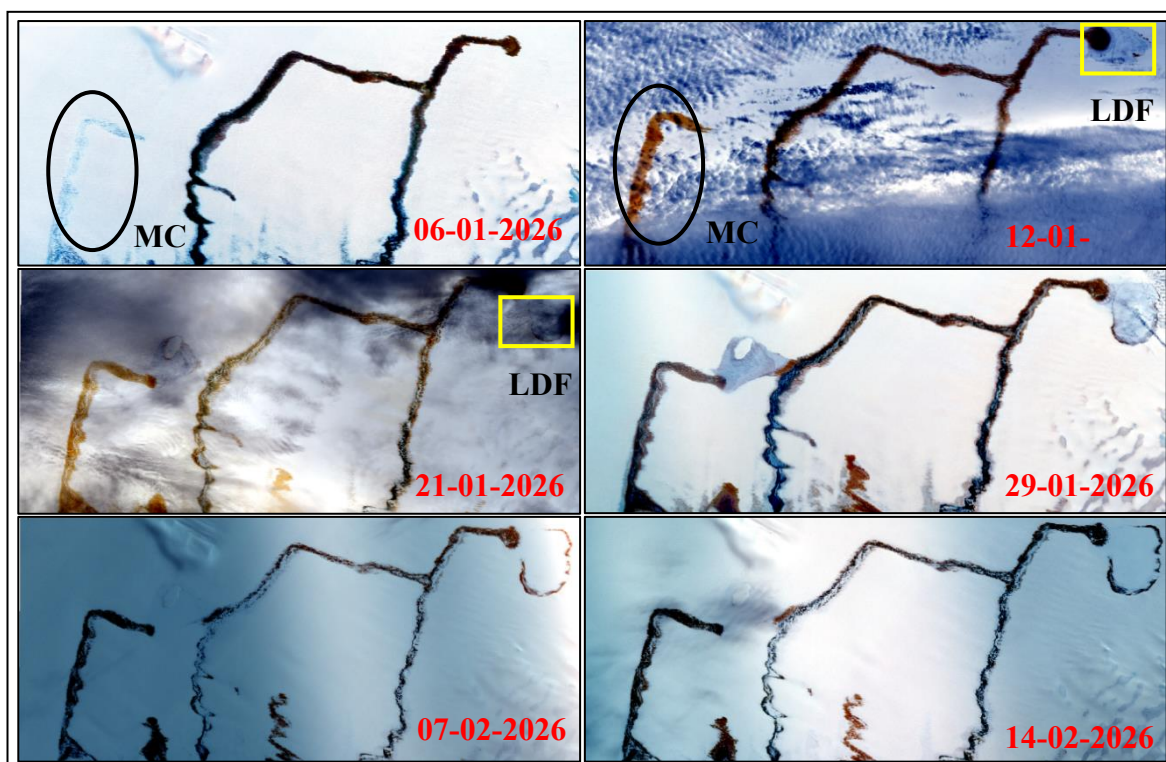
633 Overall, the system exhibits a two-tiered behavior, a persistent structural drainage template
634 (observed in SAR since 2015) and a transient, energy controlled hydrological response
635 (observed in optical data during 2026). This decoupling demonstrates that enhanced meltwater
636 energy can activate dormant pathways and generate localized stress concentrations, providing
637 a mechanistic link between surface hydrology and early-stage ice shelf destabilization.

638

639

640

641



642

643 **Figure 8.** Time series of a localized drainage feature (LDF) derived from Landsat-8/9 optical
 644 imagery (path 165/166, row 110), illustrating initiation, channel evolution, and melt channel
 645 (MC) formation between January and February 2026; sinuous supraglacial meltwater pathways
 646 appear as cerulean vein features in optical imagery.

647

648 7. Discussion

649 7.1 Synoptic drivers: localized "wells" vs. network wide loading

650 The evolution of the NIS hydrological regime is defined by a transition from isolated
 651 geometric anomalies to large scale synoptic synchronization. Historically, literature has
 652 focused on "moulin-like" features as the primary drivers of hydrofracture. Our data confirms
 653 this in 2017, where P10 functioned as a steep sided "well," reaching an extreme depth of h_{\max}
 654 = 6.92 m. This localized peak produced a hydrostatic pressure bulb (67.93 kPa) comparable to
 655 the precursor volumes observed before the 2002 Larsen B collapse (T. A. Scambos et al., 2000).
 656 However, the January 2026 event introduces a more dangerous modality. Rather than localized
 657 depth in a single "well," we observed a simultaneous expansion across extensive ponds like P2,
 658 P3, P4, and P8. This network wide pulse, yielding a $E_n = 97.81 \text{ MJ m}^{-1}$, mirrors the synoptic
 659 "melt-pulses" that destabilized the Conger Ice Shelf in 2022 (Walker et al., 1924). While P10
 660 represents a point source threat, the 2026 synchronization represents a perforated hinge line

661 across the entire grounding zone, a signature of the intensified Atmospheric River (AR) activity
662 now dominating East Antarctic shelf dynamics (Onz et al., 2024).

663 **7.2 The "Firn-poor" paradox and tidal priming**

664 Nivlisen exhibits a mechanical vulnerability that exceeds the classic Peninsula models.
665 In the Larsen B and Wilkins systems, a decades long depletion of the firn layer preceded
666 collapse (Glasser & Scambos, 2008). In contrast, Nivlisen's status as a BIA means it operates
667 with near-zero Firn Air Content (FAC) (Stevens et al., 2024; Veldhuijsen et al., 2024)
668 With a depth averaged density of 850 kg m^{-3} , the NIS behaves as a non-porous, brittle slab
669 (Humbert et al., 2009). In "firn-rich" shelves, up to 50% of meltwater is sequestered in pores,
670 dampening crack tip stress (Wessem et al., 2018). At Nivlisen, the hydrostatic loads we
671 measured peaking at $K_{\text{water}} = 0.8204 \text{ MPa m}^{1/2}$ are transmitted with 100% efficiency to the ice
672 skeleton. This loading is further aggravated by tidal fatigue. As demonstrated by Macayeal et
673 al., (2015) & R.T. Walker et al., (2013), cyclic tidal bending within the flexural hinge ($< 3 \text{ km}$
674 from the grounding line) "primes" the ice with micro fractures. This effectively lowers the
675 fracture toughness (K_{Ic}) threshold, making our recorded K_{total} of $0.61 \text{ MPa m}^{1/2}$ a definitive
676 driver for through cutting rifts.

677 **7.3 Cascading instability: Nivlisen's tipping point**

678 The synchronization of high stress intensities in 2026 suggests the NIS has reached the
679 threshold for Lake Induced Chain Reactions (LICR). When extensive ponds like P8 (0.4527
680 $\text{MPa m}^{1/2}$) and P9 ($0.5155 \text{ MPa m}^{1/2}$) exceed the $0.4 \text{ MPa m}^{1/2}$ threshold simultaneously, the
681 "mechanical safety bridges" between ponds fail.

682 This transition from the isolated "well" mechanics of P10 to the network scale stress of 2026
683 mirrors the cascading drainage events that led to rapid fragmentation in the Antarctic Peninsula
684 (Bevan et al., 2020; Lhermitte et al., 2020). Without a firm "sponge" to arrest crack propagation,
685 the "wedge effect" of synchronized surface water becomes the dominant mass loss mechanism.
686 As modeled by Winkelmann et al., (2026), East Antarctic shelves are no longer "stable"
687 outliers, our numerical results show that Nivlisen is now susceptible to the same non-linear
688 disintegration patterns that claimed the Wilkins and Larsen B shelves (Banwell et al., 2013; T.
689 A. Scambos et al., 2000).

690 **7.4 Scope and limitations**

691 While this assessment provides a robust decadal perspective, the results are subject to
692 six specific constraints: (1) Temporal resolution, where the 16 day Landsat repeat cycle may
693 miss transient peak meltwater signals, (2) Model dimensionality, as the 1D Euler-Bernoulli

694 framework simplifies lateral stress transfers, (3) Spatial averaging, which ISEA-44 validation
695 identified as a 27.6% negative bias in satellite depth retrievals, (4) Oceanic coupling, as the
696 exclusion of basal melt ($0.2\text{--}1.5\text{ m yr}^{-1}$) neglects the structural weakening caused by ice
697 thinning, (5) Material properties, specifically the assumption of a constant 850 kg m^{-3} density,
698 and (6) Flexural rigidity, as our purely elastic treatment neglects potential viscoelastic
699 deformation during prolonged ponding (Lindbäck et al., 2015). By acknowledging these
700 factors, we emphasize that our reported stress intensities are conservative lower bounds,
701 ensuring that the identified threats to the NIS are reported with high confidence and zero
702 overestimation.

703 **7.5 Field validation and scale constraints (ISEA-44)**

704 To evaluate the reliability of the Landsat-8, 9 retrieval algorithm, in-situ validation was
705 conducted during the ISEA-44 in January 2025 (Field photograph Figure 9 and Table 13). Due
706 to logistical and safety constraints, a representative melt pond near the grounding line was
707 selected for instrumentation. Although this pond's diameter was $< 250\text{ m}$ (excluding it from the
708 primary 11 year time series), its location within the same glaciological sector provides a robust
709 proxy for sensor performance.

710 Continuous 15 minute monitoring using a Keller DCX-22 Pressure Transducer Assembly
711 (PTA) on 9 January 2025 recorded a peak hydrostatic head of 1.63 m (160 mbar). After
712 temporal aggregation and averaging to synchronize with the satellite overpass, the coincident
713 30 m Landsat pixel yielded a depth of 1.2 m ($11,542.9\text{ Pa}$). This 27.6% underestimation is
714 attributed to spatial averaging, the PTA measures the water column at a single point, whereas
715 the satellite integrates depth across a 900 m^2 footprint. Despite this offset, the high degree of
716 temporal correlation indicates that satellite derived data provides a reliable, albeit conservative,
717 basis for monitoring hydraulic loading.

718
719
720
721
722
723
724
725
726
727
728



729 **Figure 9.** Field deployment (-70.7722, 11.8772) of PTA during ISEA-44 (January 2025) over
730 a supraglacial melt pond near the grounding line.

731 **Table 13.** Field validation metrics obtained on 9 January 2025.

Metric	Field Measurement (PTA)	Landsat-8 Estimate	Difference (L8 – Field)	Assessment
Hydropressure	16,000 Pa	11,542.9 Pa	-4,457.1 Pa	Pressure bias = -4.46 kPa
Pond Depth	1.63 m	1.18 m	-0.45 m	Depth bias = -0.45 m
Absolute Depth Error	—	—	0.45 m	MAE (single point) = 0.45 m
Relative Depth Error	—	—	—	27.6% underestimation

732

733 7.6 Comprehensive uncertainty analysis and error propagation

734 The assessment of hydrofracture potential involves a multi source uncertainty budget.
735 To ensure the reliability of our findings, we account for observational and parameter
736 uncertainties using a first order Root Sum Square (RSS) framework as in equation (5):

737
738
739

$$\sigma_{K_{total}} = \sqrt{\sigma_{obs}^2 + \sigma_{param}^2} \quad (5)$$

740 **7.6.1 Observational uncertainty (σ_{obs})**

741 The primary observational variance stems from the 30 m pixel averaging identified
742 during ISEA-44. Our validation shows a depth underestimation of 0.43 m (27.6%). At the 2017
743 peak depth of $h = 6.92$ m, this corresponds to a stress intensity uncertainty of ± 0.048 MPa $\text{m}^{1/2}$.
744 Because the satellite derived pressure (115.4 mbar) is consistently lower than the field
745 measured pressure (160 mbar), this error is treated as a systematic negative bias. Consequently,
746 our K_{total} values are reported as conservative lower-bounds.

747 **7.6.2 Material parameter sensitivity (σ_{param})**

748 Uncertainty in ice density ($\rho_i = 850 \pm 42.5$ kg m^{-3}) influences the lithostatic overburden
749 (K_{litho}). Sensitivity analysis reveals that a 5% shift in density alters K_{total} by only ± 0.015 MPa
750 $\text{m}^{1/2}$. Even when compounding this with the depth uncertainty, the aggregate RSS error remains
751 approximately $\pm 8.2\%$. Crucially, our peak stress intensity (0.61 MPa $\text{m}^{1/2}$) remains robustly
752 above the fracture toughness threshold (0.1-0.4 MPa $\text{m}^{1/2}$), ensuring the mechanical verdict is
753 statistically sound.

754 **7.6.3 Structural and temporal considerations**

755 While a specific numerical value for structural uncertainty (1D vs. 2D modeling) was
756 not estimated in this study, it is acknowledged that 1D Euler-Bernoulli models typically
757 provide a simplified representation of hinge zone flexure. However, by ignoring the
758 "perforation effect" of multiple synchronized ponds, the 1D approach likely underestimates the
759 total shelf fragility. Furthermore, the low RMSE (0.32 m) between the 15 minute PTA field
760 data and satellite overpasses indicates that the temporal synchronization of the study is highly
761 reliable, effectively capturing the seasonal hydraulic pulses.

762 **8. Conclusion**

763 The NIS has entered a period of structural instability. Our 11 year assessment proves
764 that the era of isolated, "safe" surface melting has ended, replaced by synchronized events that
765 mechanically overwhelm the grounding zone.

766 The evidence is twofold, first, the 2026 event proves the shelf is vulnerable to regional scale
767 hydraulic loading. Second, our ISEA-44 validation confirms that these risks are being
768 systematically underestimated by remote sensing alone. Because Nivlisen lacks a protective
769 firm buffer, it is hypersensitive to the intensifying moisture transport hitting the East Antarctic
770 coast. We conclude that the NIS is currently a high risk sector for lake induced hydrofracture.
771 Without urgent, high resolution monitoring of these "wedge-like" ponding events, the eventual
772 disintegration of this hinge zone may occur with little further warning.

773

774 **Acknowledgement**

775 The authors acknowledge the logistical support given by the National Centre for Polar
776 and Ocean Research (NCPOR), Ministry of Earth Sciences (MOES), Govt. of India (GoI)
777 under the Indian Scientific Expedition to Antarctica (ISEA) with project code 42-AMOS/OR-
778 06(2) and 44-RSG/OR-01(2) to undertake this research. The authors gratefully acknowledge
779 the support rendered by PTICL and TITCL. This work has been made possible through the
780 dedicated support of our Director and Sringeri Sharada Peetham, Sringeri, whose commitment
781 to polar science is unwavering. Satellite observations used in this study were accessed through
782 the U.S. Geological Survey and the Alaska Satellite Facility via NASA Earthdata.

783 **Declaration of Generative AI and AI-assisted technologies in the writing process:**

784 During the preparation of this work, the authors used ChatGPT 5 to assist with rephrasing and
785 improving the clarity of the manuscript's language. All content was carefully reviewed and
786 edited by the authors to ensure its accuracy and completeness. The authors take full
787 responsibility for the final version of the publication.

788 **Competing interest**

789 All the authors declare they have no conflict of interest.

790 **Financial Support**

791 This project was supported by the National Centre for Polar and Ocean Research (NCPOR),
792 Ministry of Earth Sciences, Government of India, under India's Antarctica program. No direct
793 fundings were provided.

794 **Data Availability**

795 Data available on request.

796

797

798

799

800

801

802 **References**

- 803 Alley, R. B., Dupont, T. K., Parizek, B. R., & Anandakrishnan, S. (2005). *Access of surface*
804 *meltwater to beds of sub-freezing glaciers : preliminary insights*. 8–14.
- 805 Anderson, T. L. (2017). *Fracture Mechanics: Fundamentals and Applications*.
- 806 Arthur, J. F., Stokes, C. R., Jamieson, S. S. R., Carr, R. J., & Leeson, A. A. (2020).
807 Distribution and seasonal evolution of supraglacial lakes on Shackleton Ice Shelf, East
808 Antarctica. *Cryosphere*, 14(11), 4103–4120. <https://doi.org/10.5194/tc-14-4103-2020>
- 809 Ayeal, D. R. M., Scambos, T. A., Hulbe, C. L., & Fahnestock, M. A. (2003). *Catastrophic*
810 *ice-shelf break-up by an ice-shelf-fragment-capsize mechanism*. 49.
- 811 Banwell, A. F., Macayeal, D. R., & Sergienko, O. V. (2013). Breakup of the Larsen B Ice
812 Shelf triggered by chain reaction drainage of supraglacial lakes. *Advancing Earth and*
813 *Space Sciences**advancing Earth and Space Sciences*, 40(August), 5872–5876.
814 <https://doi.org/10.1002/2013GL057694>
- 815 Bell, R. E., Banwell, A. F., Trusel, L. D., & Kingslake, J. (2018). Antarctic surface hydrology
816 and impacts on ice-sheet mass balance. *Nature Climate Change*, 8(12), 1044–1052.
817 <https://doi.org/10.1038/s41558-018-0326-3>
- 818 Bell, R. E., Chu, W., Kingslake, J., Das, I., Tedesco, M., Tinto, K. J., Zappa, C. J., Frezzotti,
819 M., Boghosian, A., & Lee, W. S. (2017). Antarctic ice shelf potentially stabilized by
820 export of meltwater in surface river. *Nature Publishing Group*, 544(7650), 344–348.
821 <https://doi.org/10.1038/nature22048>
- 822 Bevan, S., Luckman, A., Hendon, H., & Wang, G. (2020). *The 2020 Larsen C Ice Shelf*
823 *surface melt is a 40-year record high*. 3551–3564.
- 824 CUFFEY, K. M. and W. S. B. P. (2011). CUFFEY, K.M. and W.S.B. PATERSON. 2010.
825 *Journal of Glaciology*, 57(202), 383–384.
826 <https://doi.org/doi:10.3189/002214311796405906>
- 827 G. Holdsworth. (1969). Flexure of a floating ice tongue*. *Journal of Glaciology*, 8(54).
828 <https://doi.org/DOI:10.1017/S0022143000013319>
- 829 Geetha Priya, M., Raghavendra, K. R., Dhanush, S., Rakshita, C., Mahesh, B., & Deva
830 Jefflin, A. R. (2024). Monitoring of melt ponds and supra-glacial lakes over Nivlisen Ice

- 831 Shelf, East Antarctica, using satellite-based multispectral data. *Civil Engineering*
832 *Innovations for Sustainable Communities with Net Zero Targets*, 297–308.
833 <https://doi.org/10.1201/9781032686899-24>
- 834 Glasser, N. F., & Scambos, T. A. (2008). *A structural glaciological analysis of the 2002*
835 *Larsen B ice-shelf collapse*. 54(184), 3–16.
- 836 Humbert, A., Kleiner, T., Mohrholz, C., Oelke, C., Greve, R., & Lange, M. A. (2009). *A*
837 *comparative modeling study of the Brunt Ice Shelf / Stancomb-Wills Ice Tongue system*,
838 *East Antarctica*. 55(189), 53–65.
- 839 Jonathan Kingslake, E. a. (2017). Widespread movement of meltwater onto and across
840 Antarctic ice shelves. *Nature Publishing Group*, 544(7650), 349–352.
841 <https://doi.org/10.1038/nature22049>
- 842 K. Mahalinganathan et.al. (2011). Relation between surface topography and sea-salt snow
843 chemistry from Princess Elizabeth Land, East Antarctica. *The Cryosphere*, 2967–2989.
844 <https://doi.org/10.5194/tcd-5-2967-2011>
- 845 Krawczynski, M. J., Behn, M. D., Das, S. B., & Joughin, I. (2009). Constraints on the lake
846 volume required for hydro-fracture through ice sheets. *Advancing Earth and Space*
847 *Sciences* *Advancing Earth and Space Sciences*, 36(April), 1–5.
848 <https://doi.org/10.1029/2008GL036765>
- 849 Lai, C. Y., Kingslake, J., Wearing, M. G., Chen, P. H. C., Gentine, P., Li, H., Spergel, J. J., &
850 van Wessem, J. M. (2020). Vulnerability of Antarctica’s ice shelves to meltwater-driven
851 fracture. *Nature*, 584(7822), 574–578. <https://doi.org/10.1038/s41586-020-2627-8>
- 852 Langley, E. S., Leeson, A. A., Stokes, C. R., & Jamieson, S. S. R. (n.d.). *Seasonal Evolution*
853 *of Supraglacial Lakes on an East Antarctic Outlet Glacier*.
854 <https://doi.org/10.1002/2016GL069511>
- 855 Lhermitte, S., Sun, S., Shuman, C., Wouters, B., Pattyn, F., & Wuite, J. (2020). *Damage*
856 *accelerates ice shelf instability and mass loss in Amundsen Sea Embayment*. 117(40),
857 24735–24741. <https://doi.org/10.1073/pnas.1912890117>
- 858 Lindbäck et al. (2015). Subglacial water drainage, storage, and piracy beneath the Greenland
859 ice sheet. *Geophysical Research Letters*, 42(18), 1–12.
860 <https://doi.org/10.1002/2015GL065393>

- 861 M, G. P., R, D. J. A., Luis, A. J., & Bahuguna, I. M. (2022). *Estimation of surface melt*
862 *induced melt pond depths over Amery Ice Shelf , East Antarctica using Multispectral*
863 *and ICESat-2 data. 15(8), 1–8.*
- 864 M, G. P., & Venkatesh, K. (2024). Exploring the frozen frontier : unmanned aerial vehicles
865 and multispectral sensors unveiling cryosphere dynamics in East Antarctica ’ s Dronning
866 Maud Land. *GIScience & Remote Sensing, 61(1).*
867 <https://doi.org/10.1080/15481603.2024.2302739>
- 868 Morlighem, M., Rignot, E., Binder, T., Blankenship, D., Drews, R., Eagles, G., Eisen, O.,
869 Ferraccioli, F., Forsberg, R., Fretwell, P., Goel, V., Greenbaum, J. S., Gudmundsson, H.,
870 Guo, J., Helm, V., Hofstede, C., Howat, I., Humbert, A., Jokat, W., ... Smith, E. C.
871 (2019). Deep glacial troughs and stabilizing ridges ice sheet. *Nature Geoscience, 13,*
872 *132–137.* <https://doi.org/10.1038/s41561-019-0510-8>
- 873 Murugesan, G. P., Koppuram Ramesh Babu, R., Baineni, M., Chidananda, R., Satish, D.,
874 Sivalingam, S., Aruldas, D. J., Venkatesh, K., Muniswamy, N. K., & Luis, A. J.
875 (2023). Decoding the Dynamics of Climate Change Impact: Temporal Patterns of
876 Surface Warming and Melting on the Nivlisen Ice Shelf, Dronning Maud Land, East
877 Antarctica. *Remote Sensing, 15(24).* <https://doi.org/10.3390/rs15245676>
- 878 Murugesan, G.P., Satish, D., Ramesh Babu, R., Baineni, M., Chidananda, R. (2025). Surface
879 Melt Assessment of Nivlisen Ice Shelf, East Antarctica via SAR Satellite Data Analysis
880 During Austral Summer 2022–2023. In: Shukla, P.K., Bhatt, A., Mittal, H., Engelbrecht,
881 A. (eds) Computer Vision and Robotics. CVR 2024. Algorithms for Intelligent Systems.
882 Springer, Singapore. https://doi.org/10.1007/978-981-97-8868-2_10
- 883 Nimmo, F. (2004). *THE YOUNG’S MODULUS OF ICE (2004).*
884 <https://doi.org/10.1029/2002GL016660>
- 885 Onz, S. E. G., Errero, Á. L. E. Z., Einrich, V. I. J. H., Ubert, G. U. H., Oos, H. A. J., Eong, S.,
886 Im, O. K., Mith, I. N. G. A. J. S., Prenger, M. I. S., Rusel, L. U. K. E. T., Dy, D. A. U.,
887 Ance, T. E. V, & Ignon, É. T. V. (2024). *The Extraordinary March 2022 East*
888 *Antarctica “ Heat ” Wave . Part I : Observations and Meteorological Drivers. March*
889 *2022, 757–778.* <https://doi.org/10.1175/JCLI-D-23-0175.1>
- 890 Pollard, D., & Deconto, R. M. (2016). Contribution of Antarctica to past and future sea-level
891 rise. *Nature, 531(7596), 591–597.* <https://doi.org/10.1038/nature17145>

- 892 Rist, M. A., Sammonds, P. R., & Oerter, H. (2002). *Fracture of Antarctic shelf ice*.
893 *107*(January).
- 894 Scambos, T. A., Bohlander, J. A., Shuman, C. A., & Skvarca, P. (2004). *Glacier acceleration*
895 *and thinning after ice shelf collapse in the Larsen B embayment , Antarctica*.
896 *31*(December 2001), 2001–2004. <https://doi.org/10.1029/2004GL020670>
- 897 Scambos, T. A., Hulbe, C., Fahnestock, M., & Bohlander, J. (2000). *The link between climate*
898 *warming and break-up of ice shelves in the Antarctic Peninsula*. *46*(1996).
- 899 Scambos, T., Amanda, H., Liu, C., Bohlander, J., Fastook, J., Sargent, A., Massom, R., &
900 Wu, A. (2009). Ice shelf disintegration by plate bending and hydro-fracture : Satellite
901 observations and model results of the 2008 Wilkins ice shelf break-ups. *Earth and*
902 *Planetary Science Letters*, *280*(1–4), 51–60. <https://doi.org/10.1016/j.epsl.2008.12.027>
- 903 SCHULSON, E. M. and P. D. 2009. (2011). Creep and fracture of ice. *Journal of Glaciology*,
904 *57*(202), 385–386. <https://doi.org/10.3189/S0022143000206254>
- 905 Sinharay, R. K. (2022). Ground Penetrating Radar (GPR) survey over a melting blue ice
906 area (BIA) at the south of Schirmacher Oasis , Dronning Maud Land , East Antarctica.
907 *Polar Science*, *32*(June 2021), 100845. <https://doi.org/10.1016/j.polar.2022.100845>
- 908 Stevens, C. M., Sass, L., Florentine, C., McNeil, C., Baker, E., & Bollen, K. (2024). Direct
909 measurements of firn-density evolution from 2016 to 2022 at Wolverine Glacier,
910 Alaska. *Journal of Glaciology*, *70*. <https://doi.org/10.1017/jog.2024.24>
- 911 Stokes, C. R., Sanderson, J. E., Miles, B. W. J., Jamieson, S. S. R., & Leeson, A. A. (2019).
912 Widespread distribution of supraglacial lakes around the margin of the East Antarctic
913 Ice Sheet. *Scientific Reports*, *September*, 1–14. [https://doi.org/10.1038/s41598-019-](https://doi.org/10.1038/s41598-019-50343-5)
914 [50343-5](https://doi.org/10.1038/s41598-019-50343-5)
- 915 Vaughan, D. G. (1995). Southem. *Journal of Geophysical Research*, *100*(Figure 1), 6213–
916 6224. <https://doi.org/doi:10.1029/94JB02467>
- 917 Veen, C. J. Van Der. (1998). *Fracture mechanics approach to penetration of bottom*
918 *crevasses on glaciers*. 213–223.
- 919 Veldhuijsen, S. B. M., Van De Berg, W. J., Kuipers Munneke, P., & Van Den Broeke, M. R.
920 (2024). Firn air content changes on Antarctic ice shelves under three future warming
921 scenarios. *Cryosphere*, *18*(4), 1983–1999. <https://doi.org/10.5194/tc-18-1983-2024>

- 922 Walker, C., Millstein, J., Miles, B., Cook, S., & Fricker, H. A. (1924). *The Multi-decadal*
923 *Collapse of East Antarctica 's Conger-Glenzer Ice Shelf*.
- 924 Wesse, J. M. Van, Berg, W. J. Van De, Noël, B. P. Y., Meijgaard, E. Van, Amory, C.,
925 Birnbaum, G., Jakobs, C. L., Krüger, K., Lenaerts, J. T. M., Lhermitte, S., Ulft, L. H.
926 Van, Wouters, B., Wuite, J., & Broeke, M. R. Van Den. (2018). *Modelling the climate*
927 *and surface mass balance of polar ice sheets using RACMO2 – Part 2 : Antarctica (*
928 *1979 – 2016)*. 1479–1498.
- 929 Alley, R. B., Dupont, T. K., Parizek, B. R., & Anandakrishnan, S. (2005). *Access of surface*
930 *meltwater to beds of sub-freezing glaciers : preliminary insights*. 8–14.
- 931 Anderson, T. L. (2017). *Fracture Mechanics: Fundamentals and Applications*.
- 932 Arthur, J. F., Stokes, C. R., Jamieson, S. S. R., Carr, R. J., & Leeson, A. A. (2020).
933 Distribution and seasonal evolution of supraglacial lakes on Shackleton Ice Shelf, East
934 Antarctica. *Cryosphere*, 14(11), 4103–4120. <https://doi.org/10.5194/tc-14-4103-2020>
- 935 Ayeal, D. R. M., Scambos, T. A., Hulbe, C. L., & Fahnestock, M. A. (2003). *Catastrophic*
936 *ice-shelf break-up by an ice-shelf-fragment-capsize mechanism*. 49.
- 937 Banwell, A. F., Macayeal, D. R., & Sergienko, O. V. (2013). Breakup of the Larsen B Ice
938 Shelf triggered by chain reaction drainage of supraglacial lakes. *Advancing Earth and*
939 *Space Sciences* *Advancing Earth and Space Sciences*, 40(August), 5872–5876.
940 <https://doi.org/10.1002/2013GL057694>
- 941 Bell, R. E., Banwell, A. F., Trusel, L. D., & Kingslake, J. (2018). Antarctic surface hydrology
942 and impacts on ice-sheet mass balance. *Nature Climate Change*, 8(12), 1044–1052.
943 <https://doi.org/10.1038/s41558-018-0326-3>
- 944 Bell, R. E., Chu, W., Kingslake, J., Das, I., Tedesco, M., Tinto, K. J., Zappa, C. J., Frezzotti,
945 M., Boghosian, A., & Lee, W. S. (2017). Antarctic ice shelf potentially stabilized by
946 export of meltwater in surface river. *Nature Publishing Group*, 544(7650), 344–348.
947 <https://doi.org/10.1038/nature22048>
- 948 Bevan, S., Luckman, A., Hendon, H., & Wang, G. (2020). *The 2020 Larsen C Ice Shelf*
949 *surface melt is a 40-year record high*. 3551–3564.
- 950 CUFFEY, K. M. and W. S. B. P. (2011). CUFFEY, K.M. and W.S.B. PATERSON. 2010.
951 *Journal of Glaciology*, 57(202), 383–384.

- 952 <https://doi.org/doi:10.3189/002214311796405906>
- 953 G. Holdsworth. (1969). Flexure of a floating ice tongue*. *Journal of Glaciology*, 8(54).
- 954 <https://doi.org/DOI:10.1017/S0022143000013319>
- 955 Geetha Priya, M., Raghavendra, K. R., Dhanush, S., Rakshita, C., Mahesh, B., & Deva
956 Jefflin, A. R. (2024). Monitoring of melt ponds and supra-glacial lakes over Nivlisen Ice
957 Shelf, East Antarctica, using satellite-based multispectral data. *Civil Engineering
958 Innovations for Sustainable Communities with Net Zero Targets*, 297–308.
959 <https://doi.org/10.1201/9781032686899-24>
- 960 Glasser, N. F., & Scambos, T. A. (2008). *A structural glaciological analysis of the 2002
961 Larsen B ice-shelf collapse*. 54(184), 3–16.
- 962 Humbert, A., Kleiner, T., Mohrholz, C., Oelke, C., Greve, R., & Lange, M. A. (2009). *A
963 comparative modeling study of the Brunt Ice Shelf / Stancomb-Wills Ice Tongue system ,
964 East Antarctica*. 55(189), 53–65.
- 965 Jonathan Kingslake, E. a. (2017). Widespread movement of meltwater onto and across
966 Antarctic ice shelves. *Nature Publishing Group*, 544(7650), 349–352.
967 <https://doi.org/10.1038/nature22049>
- 968 K. Mahalinganathan et.al. (2011). Relation between surface topography and sea-salt snow
969 chemistry from Princess Elizabeth Land, East Antarctica. *The Cryosphere*, 2967–2989.
970 <https://doi.org/10.5194/tcd-5-2967-2011>
- 971 Krawczynski, M. J., Behn, M. D., Das, S. B., & Joughin, I. (2009). Constraints on the lake
972 volume required for hydro-fracture through ice sheets. *Advancing Earth and Space
973 Sciencesadvancing Earth and Space Sciences*, 36(April), 1–5.
974 <https://doi.org/10.1029/2008GL036765>
- 975 Lai, C. Y., Kingslake, J., Wearing, M. G., Chen, P. H. C., Gentine, P., Li, H., Spergel, J. J., &
976 van Wessem, J. M. (2020). Vulnerability of Antarctica’s ice shelves to meltwater-driven
977 fracture. *Nature*, 584(7822), 574–578. <https://doi.org/10.1038/s41586-020-2627-8>
- 978 Langley, E. S., Leeson, A. A., Stokes, C. R., & Jamieson, S. S. R. (n.d.). *Seasonal Evolution
979 of Supraglacial Lakes on an East Antarctic Outlet Glacier*.
980 <https://doi.org/10.1002/2016GL069511>
- 981 Lhermitte, S., Sun, S., Shuman, C., Wouters, B., Pattyn, F., & Wuite, J. (2020). *Damage*

- 982 *accelerates ice shelf instability and mass loss in Amundsen Sea Embayment. 117(40),*
983 24735–24741. <https://doi.org/10.1073/pnas.1912890117>
- 984 Lindbäck et al. (2015). Subglacial water drainage, storage, and piracy beneath the Greenland
985 ice sheet. *Geophysical Research Letters*, 42(18), 1–12.
986 <https://doi.org/10.1002/2015GL065393>
- 987 M, G. P., R, D. J. A., Luis, A. J., & Bahuguna, I. M. (2022). *Estimation of surface melt*
988 *induced melt pond depths over Amery Ice Shelf , East Antarctica using Multispectral*
989 *and ICESat-2 data. 15(8), 1–8.*
- 990 M, G. P., & Venkatesh, K. (2024). Exploring the frozen frontier : unmanned aerial vehicles
991 and multispectral sensors unveiling cryosphere dynamics in East Antarctica ’ s Dronning
992 Maud Land. *GIScience & Remote Sensing*, 61(1).
993 <https://doi.org/10.1080/15481603.2024.2302739>
- 994 Morlighem, M., Rignot, E., Binder, T., Blankenship, D., Drews, R., Eagles, G., Eisen, O.,
995 Ferraccioli, F., Forsberg, R., Fretwell, P., Goel, V., Greenbaum, J. S., Gudmundsson, H.,
996 Guo, J., Helm, V., Hofstede, C., Howat, I., Humbert, A., Jokat, W., ... Smith, E. C.
997 (2019). Deep glacial troughs and stabilizing ridges ice sheet. *Nature Geoscience*, 13,
998 132–137. <https://doi.org/10.1038/s41561-019-0510-8>
- 999 Murugesan, G. P., Koppuram Ramesh Babu, R., Baineni, M., Chidananda, R., Satish, D.,
1000 Sivalingam, S., Aruldas, D. J., Venkatesh, K., Muniswamy, N. K., & Luis, A. J.
1001 (2023). Decoding the Dynamics of Climate Change Impact: Temporal Patterns of
1002 Surface Warming and Melting on the Nivlisen Ice Shelf, Dronning Maud Land, East
1003 Antarctica. *Remote Sensing*, 15(24). <https://doi.org/10.3390/rs15245676>
- 1004 Nimmo, F. (2004). *THE YOUNG’S MODULUS OF ICE (2004)*.
1005 <https://doi.org/10.1029/2002GL016660>
- 1006 Onz, S. E. G., Errero, Á. L. E. Z., Einrich, V. I. J. H., Ubert, G. U. H., Oos, H. A. J., Eong, S.,
1007 Im, O. K., Mith, I. N. G. A. J. S., Prenger, M. I. S., Rusel, L. U. K. E. T., Dy, D. A. U.,
1008 Ance, T. E. V, & Ignon, É. T. V. (2024). *The Extraordinary March 2022 East*
1009 *Antarctica “ Heat ” Wave . Part I : Observations and Meteorological Drivers. March*
1010 *2022, 757–778.* <https://doi.org/10.1175/JCLI-D-23-0175.1>
- 1011 Pollard, D., & Deconto, R. M. (2016). Contribution of Antarctica to past and future sea-level

- 1012 rise. *Nature*, 531(7596), 591–597. <https://doi.org/10.1038/nature17145>
- 1013 Rist, M. A., Sammonds, P. R., & Oerter, H. (2002). *Fracture of Antarctic shelf ice*.
1014 107(January).
- 1015 Scambos, T. A., Bohlander, J. A., Shuman, C. A., & Skvarca, P. (2004). *Glacier acceleration*
1016 *and thinning after ice shelf collapse in the Larsen B embayment , Antarctica*.
1017 31(December 2001), 2001–2004. <https://doi.org/10.1029/2004GL020670>
- 1018 Scambos, T. A., Hulbe, C., Fahnestock, M., & Bohlander, J. (2000). *The link between climate*
1019 *warming and break-up of ice shelves in the Antarctic Peninsula*. 46(1996).
- 1020 Scambos, T., Amanda, H., Liu, C., Bohlander, J., Fastook, J., Sargent, A., Massom, R., &
1021 Wu, A. (2009). Ice shelf disintegration by plate bending and hydro-fracture : Satellite
1022 observations and model results of the 2008 Wilkins ice shelf break-ups. *Earth and*
1023 *Planetary Science Letters*, 280(1–4), 51–60. <https://doi.org/10.1016/j.epsl.2008.12.027>
- 1024 SCHULSON, E. M. and P. D. 2009. (2011). Creep and fracture of ice. *Journal of Glaciology*,
1025 57(202), 385–386. <https://doi.org/10.3189/S0022143000206254>
- 1026 Sinharay, R. K. (2022). Ground Penetrating Radar (GPR) survey over a melting blue ice
1027 area (BIA) at the south of Schirmacher Oasis , Dronning Maud Land , East Antarctica.
1028 *Polar Science*, 32(June 2021), 100845. <https://doi.org/10.1016/j.polar.2022.100845>
- 1029 Stevens, C. M., Sass, L., Florentine, C., McNeil, C., Baker, E., & Bollen, K. (2024). Direct
1030 measurements of firn-density evolution from 2016 to 2022 at Wolverine Glacier,
1031 Alaska. *Journal of Glaciology*, 70. <https://doi.org/10.1017/jog.2024.24>
- 1032 Stokes, C. R., Sanderson, J. E., Miles, B. W. J., Jamieson, S. S. R., & Leeson, A. A. (2019).
1033 Widespread distribution of supraglacial lakes around the margin of the East Antarctic
1034 Ice Sheet. *Scientific Reports*, September, 1–14. [https://doi.org/10.1038/s41598-019-](https://doi.org/10.1038/s41598-019-50343-5)
1035 50343-5
- 1036 Vaughan, D. G. (1995). Souther. *Journal of Geophysical Research*, 100(Figure 1), 6213–
1037 6224. <https://doi.org/doi:10.1029/94JB02467>
- 1038 Veen, C. J. Van Der. (1998). *Fracture mechanics approach to penetration of bottom*
1039 *crevasses on glaciers*. 213–223.
- 1040 Veldhuijsen, S. B. M., Van De Berg, W. J., Kuipers Munneke, P., & Van Den Broeke, M. R.

- 1041 (2024). Firn air content changes on Antarctic ice shelves under three future warming
1042 scenarios. *Cryosphere*, 18(4), 1983–1999. <https://doi.org/10.5194/tc-18-1983-2024>
- 1043 Walker, C., Millstein, J., Miles, B., Cook, S., & Fricker, H. A. (1924). *The Multi-decadal*
1044 *Collapse of East Antarctica 's Conger-Glenzer Ice Shelf*.
- 1045 Wessem, J. M. Van, Berg, W. J. Van De, Noël, B. P. Y., Meijgaard, E. Van, Amory, C.,
1046 Birnbaum, G., Jakobs, C. L., Krüger, K., Lenaerts, J. T. M., Lhermitte, S., Ulft, L. H.
1047 Van, Wouters, B., Wuite, J., & Broeke, M. R. Van Den. (2018). *Modelling the climate*
1048 *and surface mass balance of polar ice sheets using RACMO2 – Part 2 : Antarctica (*
1049 *1979 – 2016)*. 1479–1498.
- 1050